HHS Public Access

Optical Nanosensor for Intracellular and Intracranial Detection of Amyloid-Beta

Merav Antman-Passig,
Molecular Pharmacology Program, Memorial Sloan Kettering Cancer Center, New York, New York 10065, United States

Eitan Wong,
Chemical Biology Program, Memorial Sloan Kettering Cancer Center, New York, New York 10065, United States

Georgia R. Frost,
Chemical Biology Program, Memorial Sloan Kettering Cancer Center, New York, New York 10065, United States

Christian Cupo,
Department of Mechanical Engineering, Columbia University, New York, New York 10027, United States

Janki Shah,
Molecular Pharmacology Program, Memorial Sloan Kettering Cancer Center, New York, New York 10065, United States

Albert Agustinus,
Program of Pharmacology, Weill Graduate School of Medical Sciences of Cornell University, New York, New York 10065, United States

Ziyu Chen,
Program of Physiology, Biophysics, & Systems Biology, Weill Graduate School of Medical Sciences of Cornell University, New York, New York 10065, United States

Chiara Mancinelli,
Program of Pharmacology, Weill Graduate School of Medical Sciences of Cornell University, New York, New York 10065, United States

Maikel Kamel,

Corresponding Author hellerd@mskcc.org.

Sophie Davis School of Biomedical Education, CUNY School of Medicine, New York, New York 10031, United States

Thomas Li,
Chemical Biology Program, Memorial Sloan Kettering Cancer Center, New York, New York 10065, United States; Program of Neurosciences, Weill Graduate School of Medical Sciences of Cornell University, New York, New York 10065, United States

Lauren A. Jonas,
Chemical Biology Program, Memorial Sloan Kettering Cancer Center, New York, New York 10065, United States; Program of Pharmacology, Weill Graduate School of Medical Sciences of Cornell University, New York, New York 10065, United States

Yue-Ming Li,
Chemical Biology Program, Memorial Sloan Kettering Cancer Center, New York, New York 10065, United States; Program of Pharmacology and Program of Neurosciences, Weill Graduate School of Medical Sciences of Cornell University, New York, New York 10065, United States

Daniel A. Heller
Molecular Pharmacology Program, Memorial Sloan Kettering Cancer Center, New York, New York 10065, United States; Program of Pharmacology and Program of Physiology, Biophysics, & Systems Biology, Weill Graduate School of Medical Sciences of Cornell University, New York, New York 10065, United States

Abstract

Amyloid-beta (Aβ) deposition occurs in the early stages of Alzheimer's disease (AD), but the early detection of Aβ is a persistent challenge. Herein, we engineered a near-infrared optical nanosensor capable of detecting Aβ intracellularly in live cells and intracranially in vivo. The sensor is composed of single-walled carbon nanotubes functionalized with Aβ wherein Aβ-Aβ interactions drive the response. We found that the Aβ nanosensors selectively responded to Aβ via solvatochromic modulation of the near-infrared emission of the nanotube. The sensor tracked Aβ accumulation in live cells and, upon intracranial administration in a genetic model of AD, signaled distinct responses in aged mice. This technology enables the interrogation of molecular mechanisms underlying Aβ neurotoxicity in the development of AD in living systems.

Graphical Abstract
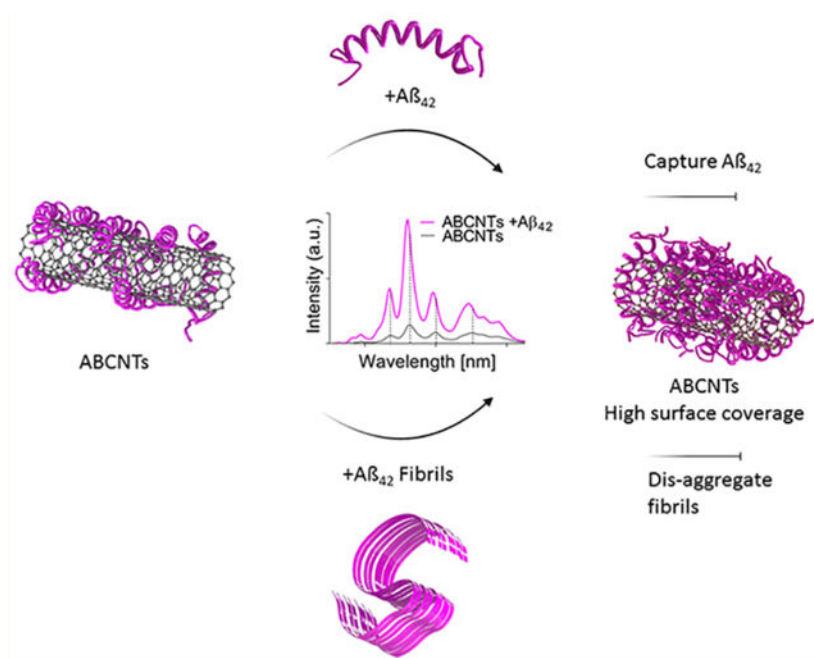
An estimated 50 million people live with Alzheimer's disease (AD) and other dementias worldwide,[1] posing an increasing global health challenge.[2] Although research aimed at providing treatments has been accelerating over the past few decades, current therapies provide minimal benefit.[3] One significant challenge[4] is the identification of early events in the initial progression of AD. The symptom-free stage of AD is accompanied by undetectable structural and molecular deformities in the brain,[5,6] characterized by amyloid-beta ($A\beta$) deposition, tau-tangle formation, and neuro-degeneration.[7]

Current hypotheses identify dyshomeostasis of $A\beta$ as a key event in AD, where the accumulation of self-aggregated $A\beta$ triggers a cascade of toxic molecular events that eventually lead to memory decline and, ultimately, advanced AD.[8,9] $A\beta$ exists in several isoforms, varying between 36 and 43 amino acids, with $A\beta_{42}$, linked to neurotoxicity and neuronal dysfunction.[10] During disease progression, $A\beta$ monomers aggregate to form oligomers and fibrils. $A\beta$ deposition is a validated signature biomarker,[7] and the change in $A\beta_{42}$ ($A\beta_{42}$: $A\beta_{40}$ ratio) is an indicator for the pathological state in AD. Preceding extracellular fibril and plaque $A\beta$ deposition, $A\beta$ may accumulate intracellularly.[11–13] Importantly, reports link intra-neuronal $A\beta$ accumulation as an initial pathogenesis event in $A\beta$-induced neurodegeneration,[14–16] along with microglia-internalized $A\beta$.[17] There is an outstanding need for tools capable of monitoring $A\beta$ accumulation intracellularly. New methods to report endogenous $A\beta$ in live cells and organisms, including intracellular accumulation of $A\beta$, could improve research efforts to elucidate mechanistic pathways that lead to $A\beta$ neurotoxicity and shed more light on the role of $A\beta$ in AD.[18,11,19,20]

The internalization of Aβ by cells is of particular importance since dysregulation of internalization, clearance, and degradation of Aβ by the neuroimmune system is a key mechanism in AD pathophysiology.[21,22] Quantitative measurements and analytical techniques to quantify Aβ have been reviewed elsewhere.[23,24] Neuroimaging modalities such as positron emission tomography and magnetic resonance imaging[25] are vital tools in the clinical setting but are limited in their ability to identify early Aβ-induced neuropathological events such as intracellular accumulation. Optical detection of Aβ with near-infrared (NIR) fluorescent imaging probes has recently enabled in vivo discovery of Aβ fibrils and, with some probes, soluble-oligomer Aβ species.[26,27] However, these imaging probes are limited by depth penetration issues[28] which constrain the detection of Aβ to the surface area of the brain. Aβ accumulation within live cells can be monitored by fluorescently tagged Aβ,[29] or by fixing cells/tissue and immunostaining with specific antibodies targeting Aβ isoforms.[30] These strategies may affect the innate Aβ bioactivity, however, and are not suitable for transient monitoring in live samples. Here, we aimed to address the need for investigative tools that can monitor Aβ subcellularly and intracranially with the capability of longitudinal and transient measurements.

One promising material class for optical biosensor development is single-walled carbon nanotubes (SWCNTs) and cylindrical carbon nanomaterials with intrinsic near-infrared-II (NIR-II) emission (1000–1700 nm) within the biological transparency window. This emission range enables deep optical penetration, reduced scattering, and low autofluorescence in tissues. SWCNTs additionally exhibit unique optical properties such as high photostability, low photobleaching, and negligible fluorescence intermittency (commonly called blinking). Noncovalent surface functionalization of SWCNTs with DNA,[31] proteins,[32–35] and polymers[36] confers demonstrable biocompatibility in living cells and animals. These properties render SWCNTs optimal for longitudinal optical measurements in live samples.[37] In this manner, optical biosensors derived from engineered SWCNTs have been developed for detecting protein biomarkers,[38] microRNA,[39] and small molecules, such as lipids,[40] in vivo. In live brain samples, SWCNT probes have been developed for imaging neurotransmitters in brain slices[41,42] and probing extracellular space in mouse brains without exhibiting obvious toxicities,[43] while amine-modified SWCNT have demonstrated neuroprotective effects in a rat stroke model.[44]

Herein, we present the development of a biosensor capable of label-free specific and sensitive detection of Aβ in live cells and animals for preclinical studies of Aβ. We functionalized SWCNTs via absorption of Aβ to the nanotube surface, utilizing the strong hydrophobic and π–π interactions between Aβ and graphitic carbon (described in refs 45–53). We hypothesized that nanotube-adsorbed Aβ would function to promote binding of endogenous Aβ, resulting in accumulation at the nanotube surface and leading to a distinct optical response. We modified carbon nanotubes with Aβ_{42}, which has a higher propensity to aggregate than Aβ_{40}.[54] We found that Aβ-functionalized SWCNTs selectively detected Aβ through modulation of their emission wavelength. In exploring the mechanism, we found that Aβ modulated the coverage on the nanotube surface, triggering a solvatochromic shift. The sensor consistently responded to synthetic and endogenous Aβ in live cells. Finally, we measured the sensor response in vivo following intracranial injection in a genetically

modified mouse model of AD, resulting in a distinct optical response that progressed with age.

RESULTS

Aβ-Functionalized Single-Walled Carbon Nanotubes Optically Respond to Aβ.

To functionalize nanotubes with Aβ, we initiated assembly of Aβ on surfactant-dispersed SWCNTs via selective displacement from precursor sodium deoxycholate-suspended nanotubes, here termed SDC-CNTs (Figure 1a). We assessed the adsorption of Aβ_{42} to the nanotube surfaces via biophysical and optical methods. Using AFM, we measured the height profiles of Aβ-functionalized carbon nanotubes (which we termed amyloid-beta carbon nanotubes, ABCNTs) revealing nanometer-sized structures with a periodic distribution distinctly different from precursor SDC-CNTs (Figure 1b,c, see Figure S1 for length distribution AFM measurements). The average height of the beadlike ridges on ABCNTs was significantly larger than fluctuations on SDC-CNTs (2.32 ± 1.48 nm vs 0.65 ± 0.42 nm, respectively) (Figure 1d). The diameters of pristine SWCNTs, as measured by AFM, range from 0.5 to 1.2 nm,[55,56] while the smallest Aβ_{42} particles are reported as globular and range between 1 and 2 nm and correspond to the monomeric form.[57,58] We therefore concluded that the beaded ridges on the nanotubes in the AFM images were adsorbed as monomeric or low-order oligomers of Aβ.

Complementing the height variation as an indication of Aβ functionalization, we found that ABCNTs exhibited a lower Young's modulus compared to SDC-CNTs (Figure S2a,b). We conclude that this attenuation upon protein derivatization is largely in concordance with a similar effect observed with DNA-CNT hybrids.[59]

We extensively characterized the optical properties of the ABCNTs. We observed well-resolved optical absorption peaks (Figure S2c) albeit increased background absorbance, suggesting that Aβ exfoliates the nanotubes adequately, but to a lesser degree than SDC.[60] In accordance, the fluorescence emission of ABCNTs was broader and shifted to longer wavelengths (i.e, red-shifted) as compared to SDC-CNTs (Figure S 2d,e).[61]

To further assess the displacement of SDC by Aβ_{42}, we measured zeta potential, which reports surface charge. We recorded a negative zeta potential of ABCNTs (Figure S2g) corresponding to the net negative charge of Aβ in alkaline solutions.[63] This result suggests that the ABCNTs are colloidally stabilized by the peptide, possibly via the hydro- phobic and π-stacking interactions between the CNT surface and hydrophobic peptide regions. We therefore surmise that charged/hydrophilic regions face the aqueous solvent to produce electrostatic repulsion between nanotube–peptide complexes.[53,64]

We investigated the interaction between the ABCNTs and Aβ_{42} by studying the optical response of ABCNTs. We hypothesized that Aβ motifs on ABCNTs would allow the capture of Aβ due to self-assembly mechanisms between molecules of Aβ.[65,66] We examined the optical response of ABCNTs to increasing concentrations of Aβ_{42}. We observed signal amplification and blue-shifting (shifting of the emission peak to shorter wavelengths) (Figure 1e,f) which fit a one- phase decay model (Figure 1g). Dose–response curves were

also acquired in response to the $A\beta_{40}$ isoform to study the differential response between isoforms (Figure S2h) and found a smaller optical wavelength shift compared to $A\beta_{42}$, indicating a higher affinity of ABCNTs to $A\beta_{42}$.

We then investigated the specificity of ABCNTs to $A\beta_{42}$ by studying the influence of biomolecules on the optical response of ABCNTs. We found a differential optical response between $A\beta_{42}$ and scrambled $A\beta_{42}$, bovine serum albumin, α-synuclein, and sphingomyelin (Figure 1h). In 10% serum, a protein biointerferent environment, we observed blue-shifted emission and increased intensity in the presence of $A\beta_{42}$ compared to scrambled $A\beta_{42}$ (Figure S2i).

To investigate the role of the ABCNT coating in the sensitivity to $A\beta_{42}$, we studied the optical responses of surfactant- and DNA-wrapped CNTs. We chose $(GT)_{15}$ and CTTCCCCTTC sequences, which have been used in multiple previous CNT sensor studies,[41,67] as well as the surfactant sodium deoxycholate (SDC), for suspension of CNTs. None of the DNA- or SDC-suspended CNTs produced similar optical responses as ABCNTs to $A\beta_{42}$, indicating a unique interaction between ABCNTs and $A\beta_{42}$ (Figure S3).

We studied the chirality-specific optical response of ABCNTs to $A\beta_{42}$ in serum (Figure S4a,b). In contemplation of the detection limit, we conducted receiver-operating characteristic (ROC) analysis of the ABCNT response to $A\beta_{42}$ and found a limit of detection of 100 nM PBS and 1 μM in 33% serum (Figure S4c,d). Due to its high signal-to-noise, low autofluorescence in biological samples, and high optical penetration, as well as the low limit of detection, we continued to investigate the (9,4) nanotube chirality as the primary sensor element. (The ABCNT optical signal hereafter refers to the (9,4) signal unless otherwise stated.)

To assess the stability of the sensor, we measured the optical properties of ABCNTs longitudinally. First, we measured ABCNT absorbance up to 14 days and found no broadening or red-shifting of the resonant absorption peaks but some decline in the fluorescence intensity (Figure S5a,b). In samples removed to a PBS solution, we found perturbations to nanotube absorption spectra (Figure S5c) and, upon incubation in 37 °C, a red-shifting response, decreased intensity, and increased full-width half-maximum (FWHM) of the emission band that was diminished by the addition of $A\beta_{42}$ (Figure S5d). In combination, these effects suggest that $A\beta$ physisorption on nanotube surfaces changed in physiological conditions.[68]

Finally, we investigated the response of surface-bound ABCNTs to $A\beta_{42}$ via spectral imaging. We found the expected blue-shifting response upon incubation with $A\beta_{42}$ (Figure S6), indicating that the responses of individual nanosensors can be imaged and that the optical modulation of the sensor by $A\beta_{42}$ was not caused by aggregation of ABCNTs.

Assembly of $A\beta_{42}$ on the Nanotube Surface Modulates Emission Wavelength.

We investigated the mechanism of the optical modulation of ABCNTs by $A\beta_{42}$. The addition of $A\beta_{42}$ results in a blue-shifted spectrum and increased intensity. Spectral blue-shifting, as observed upon addition of $A\beta_{42}$ to ABCNTs, has been linked to an increase

in nanotube surface coverage by decreasing intertube attraction.[69] Moreover, increased $A\beta$ deposition on the nanotube surface has been shown to decrease water content from the vicinity of the nanotube,[48,49] a solvatochromic phenomenon optically translated to blue-shifted emission. We therefore hypothesized that the interaction between $A\beta_{42}$ and ABCNTs results in changes to the immediate environment of nanotube surface. Further, an increase in nanotube surface coverage by $A\beta$ can derive the optical response by changing the water and polyelectrolyte exposure to the nanotube surface, resulting in a solvatochromic shift.[40]

To assess the solvatochromic response and intensity of ABCNTs in response to the dielectric environment, we measured the fluorescence intensity and wavelength upon exposure to different solvents. As expected, we identified some degree of quenching and a bathochromic (redshift) with increasing solvent polarity (Figure S7).

To determine if added $A\beta_{42}$ modulates the surface coverage of nanotubes, we visualized the adsorbed $A\beta$ on the nanotube surface with AFM (Figure 2a, Figure S8a,b). We studied the beadlike $A\beta$ structures on ABCNT's surfaces following the addition of $A\beta_{42}$ (Figure 2b) and found the mean height of the peaks increased following the addition of $A\beta_{42}$ (Figure 2c). From the relative frequency distribution (Figure S8c), we found that the probability of 4 nm elevated structures, corresponding to low molecular weight (LMW) oligomers, increased 2-fold upon the addition of $A\beta_{42}$. While the probability of 1 nm structures, roughly representing exposed nanotube surface, decreased by 40%, suggesting a decrease of exposed nanotube surface upon addition of $A\beta_{42}$.

To test if the blue-shifting response of ABCNTs can be attributed to the surface-interaction between $A\beta_{42}$ and the nanotube, we conducted a quenching experiment. We used fluorescently labeled $A\beta$ (fluor-555 $A\beta_{42}$ here designated as fluor-$A\beta$) and probed the intensity of fluor-$A\beta$ upon incubation with ABCNTs. We observed a distinct quenching effect (Figure 2d, Figure S9a), which suggests an interaction between the nanotube surface and fluor-$A\beta$, similar to quenching effects of a dye molecule in proximity to nanotube that is caused by charge-transfer events.[70,71] Since fluor-$A\beta$ may also quench upon self-association,[72,73] we further studied the quenching ratio. At low concentrations of fluor-$A\beta$ (high ABCNT: fluor-$A\beta$ ratios), we observed an increased quenching ratio (Figure S9b). The relationship between ABCNT: fluor-$A\beta$ ratio and the quenching ratio suggests ABCNTs are quenchers of the fluorophore. We also increased the ABCNT concentration with respect to $A\beta$ and plotted I_0/I versus [ABCNT] (Figure S9c), resulting in a linear plot, suggesting a primary static quenching mechanism, i.e, an association between the fluorophore (fluor-$A\beta$) and a quencher (ABCNTs), according to the Stern–Volmer plot.[74]

We then quantitatively examined the effect of ABCNTs on the rate of aggregation of $A\beta_{42}$, by measuring the fluorescence response of the thioflavin-T (ThT) dye. We found that ABCNTs did not decrease the rate of fibril formation (Figure 2e), suggesting that the association of $A\beta_{42}$ monomers or LMW oligomers to the nanotube surfaces does not prevent fibrilization. In sum, we conclude that the most probable interaction between $A\beta$ and ABCNTs is through the assembly of $A\beta_{42}$ on nanotube surfaces resulting in solvatochromic blue shifting of the emission wavelength.

Aβ-Functionalized Single-Walled Carbon Nanotubes Probe Aβ Aggregation.

We asked whether ABCNTs can optically report aggregated Aβ_{42} species. The assembly of Aβ into fibrils and the formation of oligomer-intermediate states have been studied extensively in well-defined and controlled environments. To probe ABCNT optical properties following Aβ self-assembly, we incubated ABCNTs with Aβ_{42} [10 μM] under favorable conditions for aggregation (10 μM Aβ_{42}, 37 °C, pH 7.4, 24 h) and acquired NIR emission spectra. We found a blue shift in ABCNT emission wavelength and an intensity increase (Figure 2f). A similar trend but in lower magnitude was recorded when ABCNTs were incubated with Aβ_{42} at 4 °C (Figure S10), suggesting a differential response to aggregation conditions\species, as the low temperature can slow down the formation of ordered fibrils and lead to disparate types of oligomers and fibrils.[75]

To examine whether ambient proteins will interfere with the sensitivity of the sensor during aggregation, we examined the optical shift in the presence of bovine serum albumin (BSA) since albumin is the most abundant protein in the CSF, comprising approximately 50% of total protein content.[76] We found that BSA [150 μg/mL] did not have any discernible effect on the ability of ABCNTs to distinguish between Aβ_{42} and SAβ_{42}, before and after aggregation (Figure 2g).

We studied the response of ABCNTs to aggregated states of Aβ_{42}. To quantify the optical response of ABCNT to different Aβ_{42} species, we incubated ABCNTs with Aβ_{42} prepared at monomeric, oligomer, or fibril states[75] (Figure S11). We found blue shifting and an intensity increase as a function of the fibrillar state (Figure 2g), consistent with our findings in temperature-controlled Aβ_{42} aggregation conditions.

To investigate the mechanistic pathway in which aggregated states interact with ABCNT surfaces and modulate the optical emission, we used AFM, which resolved the fibrillary form, as well as globular LMW states of Aβ_{42} (Figure S12a). Upon incubation of fibrillar Aβ_{42} with ABCNTs, we observed a decrease in fibrillar morphology and an increase in intermediate aggregate states. We quantified the change in morphology by measuring the roughness of the protein surface and found that ABCNTs lowered the surface roughness, as quantified by root-mean square (RMS) average of height deviation (Figure S12b), suggesting high fibrillary forms disassembled to lower states when incubated with ABCNTs. Concurrently, the height of ABCNTs increased compared to ABCNTs with no addition of fibrillar Aβ_{42}, suggesting that dissociated LMW Aβ accumulated on the nanotube surface (Figure S12c). To further test this hypothesis, we quantified ThT fluorescence of fibrillary Aβ_{42} following incubation with ABCNTs and found a decrease in ThT fluorescence indicating a lower prevalence of fibrillary form (Figure S12d). This finding is in line with recent studies showing that carbon nanotubes can disaggregate Aβ fibrils and adsorb dissociated Aβ_{42}.[77] We then compared the relative frequency distribution of the height of ABCNTs and found that upon incubation with fibrillar Aβ_{42} the probability of higher Aβ_{42} structures (>3 nm) on ABCNTs increased while exposed surfaces (<2 nm) decreased compared to ABCNTs incubated with freshly prepared Aβ_{42} (Figure S12e). Figure 2i illustrates the proposed mechanism and interaction between ABCNTs and Aβ_{42} in which LMW Aβ_{42} accumulates on ABCNTs, prompting a shift in the dynamic equilibrium from Aβ-Aβ association to Aβ-ABCNT association.

Aβ-Functionalized Single-Walled Carbon Nanotubes Detect Aβ in Live Cells.

We next investigated the ABCNT sensor in live cells. First, we studied the effect of ABCNTs on cell viability and found no toxic effects at up to 1 μg/mL (Figure S13a). We then examined the ABCNT response in neuronally differentiated SH-SY5Y human neuroblastoma cells,[78] a common model to study the effects of Aβ on neuronal cells. SH-SY5Y cells are susceptible to Aβ-induced toxicity caused by the accumulation of Aβ aggregates, on and within the cells.[79–81] Upon incubation, ABCNTs localized with differentiated SH-SY5Y cells. To assess the response of localized ABCNTs, we further incubated the cells with Aβ_{42}, scrambled Aβ_{42} or vehicle, and spectrally resolved the obtained images. (Figure 3a,b). We quantified ABCNT regions of interest (ROI's) and found a significant blue shift effect specifically in cells incubated with Aβ_{42} (Figure 3c).

Next, to study the response of ABCNTs in live cells, without the external addition of Aβ_{42}, we used mouse neuroblastoma cells (N2a cells) that stably overexpress amyloid precursor protein (N2a-APP) and overproduce Aβ.[82] We found that the ABCNTs proximally associated with the cells (Figure 3d), and as in the case of SH-SY5Y cells, ABCNTs associated with N2a-APP cells showed blue-shifted emission spectra compared to ABCNTs in/on WT cells (Figure 3e and Figure S13b,d,e). To investigate whether the local optical response derived from secreted Aβ, we examined the response of ABCNTs to N2a-APP conditioned media. We found that the ABCNT emission blue-shifted as compared to N2a WT conditioned media, showing that secreted Aβ can induce the expected response (Figure S13c).

Following recent reports demonstrating SWCNTs alleviate neurotoxicity and Aβ- induced toxicity in AD models,[83,84] we examined the effect of ABCNTs on toxicity in N2a cells and found that ABCNTs reduced the toxicity of Aβ (Figure 3f), likely caused by ABCNTs capturing LMW Aβ and in turn reducing the effective concentration of toxic Aβ species.

We then assessed the ability of ABCNTs to detect Aβ intracellularly. We chose a phagocytic immune cell model, human monocytic THP-1 cells differentiated into macrophages, to study ABCNTs capacity to probe Aβ_{42} intracellarly[85] as THP-1 cells have been shown to internalize Aβ[86] and respond by increasing cytokine expression.[87,88] To visualize the uptake of Aβ by the cells, we used fluor-Aβ_{42} and found that the cells internalized Aβ within a 24 h incubation time frame (Figure S14a). We then collected spectrally resolved images of the cells incubated with ABCNTs and simultaneously visualized internalized fluor-Aβ_{42} (Figure 3g). ABCNTs in the vicinity of internalized Aβ exhibited a blue shift in their emission (Figure 3h).

To determine whether the optical response of ABCNTs is linked with local intracellular Aβ_{42}, we studied the colocalization of fluorescently labeled ABCNTs (Fluor-555 Aβ_{42}) with fluor-Aβ_{42} (Fluor-488 Aβ_{42}) intracellularly. We observed colocalization of the red and green-fluorescence signals. (Figure S14b). We conclude that the ABCNT blue-shifted optical response is thus related to the local Aβ_{42} vicinity with the nanotubes.

We studied whether ABCNTs can be used as a tool to quantitatively report Aβ intracellularly. We pulsed THP-1 cells with ABCNTs and compared the optical output

following incubation with either 1 μM or 10 μM of Aβ. Both concentrations prompted a blue-shift in the emission (Figure S15a–c) without significant differences between them. This can be explained by the requirement of ABCNTs to be in the vicinity of Aβ, combined with differential uptake of Aβ by the cells (as seen in Figure S14c, with Figure S15b showing some cells highly loaded with Aβ compared to others in the same condition and Figure S15d,e showing optical emission of control samples without ABCNTs). Moreover, the intracellular effective concentration of Aβ can differ from the extracellular environment due to local concentration in vesicles.[81]

Next, we studied the ability of ABCNTs to dynamically monitor the internalization of Aβ_{42} by THP-1 cells. Spectra were collected transiently following incubation with Aβ_{42}. After 24 h of incubation, ABCNTs exhibited blue-shifted emission, consistent with previous results showing the time-dependent internalization of Aβ in cells.[81,89] Interestingly, we continued to observe blue-shifted spectra even following 5 days of incubation, accompanied by an increase in emission intensity (Figure S16).

Aβ-Functionalized Single-Walled Carbon Nanotubes Differentiate Alzheimer's Mice Model Intracranially.

Our next goal was to evaluate the utility of ABCNTs to detect Aβ locally in vivo. We used a transgenic mouse model that co-overexpresses five familial AD (FAD) mutations and produces elevated Aβ_{42} levels[14] (5XFAD). Our previous studies showed that injecting functionalized SWCNTs intravenously resulted in virtually nonexistent transfer through the blood–brain barrier (BBB) in healthy mice.[90] In this study, as a direct method to interrogate local accumulation of Aβ, we injected ABCNTs intracranially and recorded the nanotube spectra, through the intact cranium, after 24 h (schematic of the experiment shown in Figure 4a). We injected ABCNTs into the hippocampus, where Aβ_{42} accumulates as mice age[14] and where levels of soluble Aβ_{42} differ significantly from WT.[91] With these parameters, we were able to detect nanotube spectra from both the (9,4) and (8,6) chiralities in vivo (Figure 4a,b). We then compared the signal obtained in vivo from 5XFAD mice and WT. We found the (9,4) showed a significant blue-shifted effect in 5XFAD aged mice (8 months), but not in younger (4-month old) mice (Figure 4c,d). Due to the lower (8,6) signal intensity obtained from several mice we quantified the mean wavelength from ex-vivo resected brains and found similar trends (Figure S17).

To investigate the fate of ABCNTs following intracranial injection, we imaged sections from resected brains *via* NIR hyperspectral microscopy. We found a localized extracellular pool of ABCNTs in the hippocampus region, identified by the strong NIR emission (Figure 4e,f, and Figure S18). We further immunostained the slices to verify the presence of Aβ aggregates in 5XFAD mice (6E10), which also stained the pool of ABCNTs. As expected, we observed high load of Aβ aggregates in 8-month old 5XFAD mice (Figure 4e, Figure S18a). By spectrally resolving the region of ABCNTs, we found a broad distribution of nanotube emission wavelengths in the 5XFAD mice compared to WT, and overall blue-shifted (9,4) center wavelength (Figure S19a). We found lesser broadening with the (8,6) chirality, corresponding to the ex vivo results (Figure S19b). To assess the influence of ABCNTs on surrounding cells we stained sections for hematoxylin and eosin (H&E) and found no

apparent abnormalities to hippocampal tissue (Figure S20a,b). To visualize the interaction between the cells and ABCNTs we immunostained neuronal bodies (NeuN) and microglia/macrophage (Iba-1). Previous studies have shown that carbon nanoparticles negatively affect neurons[92] and that accumulation of SWCNTs in cellular organelles may lead to oxidative stress and DNA damage.[93,94] We did not however observe intracellular accumulation of ABCNTs (Figure S20cf). We then immunostained for apoptosis marker (caspase-3) (Figure S20d,g) and response to DNA damage[95] (p-53) (Figure S20e,h) finding no apparent damage to cells at the injection site. These results validate the potential of the ABCNT for in vivo use and functional intracranial sensing of Aβ.

CONCLUSIONS

Herein, we investigated the potential for an optical nanosensor to conduct label-free specific detection of Aβ in live cells and intracranially. This nanosensor took advantage of the formation of hydrophobic interactions and π–π bonds between Aβ and SWCNT to functionalize SWCNTs with Aβ. The detailed atomic interactions between SWCNTs and monomeric Aβ_{42} have been computationally studied by Zhang et al.[53] and Jana et al.[52] Luo et al. suggested a theoretical model in which carbon nanotubes are engulfed within the hydrophobic core of hollow Aβ protofibrils.[50,96] In our AFM studies, we did not find the protofibril structure characterized by ~10 nm diameters and helical repeats of ~7.8 nm[97] (Figure 1a), which can be explained by the decreased stability of such hollow core structures in the alkaline preparation conditions we have used.[98]

We determined that the sensor signal transduction mechanism is through solvatochromism and takes advantage of Aβ-Aβ association. The specific pathway in which the Aβ functionalization interacts with Aβ may involve association or exchange mechanisms. Using AFM we found disparate LMW species accumulating with the ABCNTs (Figure S12e). Previous studies[48–53] reveal that the SWCNT-Aβ_{42} binding favors Aβ conformations that increase hydrophobic and π-stacking interactions with the nanotube surface, decrease the structural stability of the peptide, and disrupt the tertiary conformation of Aβ. It is possible that by functionalizing SWCNTs with Aβ_{42} we constrained random conformations of Aβ_{42} peptide to the nanotube surface,[53] which, upon interaction with freshly prepared Aβ_{42} affect the formation and disappearance of ordered LMW oligomer species, delaying transition to organized intermediates. It is now accepted that Aβ aggregation occurs in parallel pathways, forming oligomer kinetic intermediates which can be "on-pathway" or "off- pathway" to fibril formation. Thus, the capture of LMW Aβ_{42} species on the nanotube surfaces does not necessarily affect rate of fibril formation, as we observed in our kinetic experiments (Figure 2e).[99] This capturing of LMW species on nanotube surfaces can also justify the neuroprotective effect we observed (Figure 3f). Upon incubation with fibrillary Aβ_{42} we found that ABCNTs shift the dynamic equilibrium from Aβ-Aβ association to Aβ -ABCNT association. It is also likely that the increased coverage provided by the structurally different LMW species contribute to the increased blue-shifting effect observed upon incubation with high-concentration Aβ_{42} (Figure 1g) or oligomer and fibrillary Aβ_{42} (Figure 2h).

To date, there are few methods that can target soluble Aβ_{42} LMW intermediates and enable detection of Aβ in live specimen. In vitro, we used three cell models to assess the response

of ABCNTs to Aβ transiently and in the cellular\intracellular environment. In vivo, the nanosensor detected Aβ accumulation in 5XFAD mice following intracranial injection. This study reveals functional information from a deep tissue section (2 mm), owing to the IR emission of the nanotubes. We noticed that the soluble concentration of Aβ in the extracellular environment, where the nanosensor localized at the time point that we measured, is expected to be of a lower range than detected by the nanosensor.[100,101] Our data suggests that the nanotube-based sensors disaggregate amyloid beta fibrils (Figure S12), plausibly explaining the observed optical shift from the extracellular environment, where high loading of Aβ plaques is present in dynamic equilibrium with monomeric\LMW Aβ. We speculate that this selectivity may be the reason that the nanosensor did not differentiate AD mice from WT at an earlier time point (4 months) when plaque load is lower.

We believe that the nanosensor could be readily used to facilitate mechanistic studies of Aβ accumulation, dynamics, and local intracellular clustering for disease investigations and drug pharmacodynamic studies at the cellular level. Additionally, this sensor potentially enables in vivo longitudinal monitoring of disease.

METHODS AND MATERIALS

Aβ Preparation.

All Aβ peptides were purchased from AnaSpec (CA, USA), with a purity of 95% as analyzed by% peak area by HPLC. To ensure the monomeric state of the peptide, it was dissolved in high-grade 1,1,1,3,3,3-hexafluoroisopropanol (HFIP), vortexed, and incubated at room temperature for 2 h. Aβ was then dried under a slow stream of Ar(g) and for an additional 1 h in a high vacuum to remove access HFIP. The obtained film was dissolved in 10 mM NaOH[102] (10 mM NaOH, pH ~ 10.5–11, pI of Aβ = pH 5.2,[103] or dimethyl sulfoxide (DMSO), and its concentration was determined by UV absorption using the theoretical molar extinction coefficient ε(214 nm)Aβ_{1-42} = 76848 M-1 cm-1[104,105] on a JASCOV-670 spectrophotometer. Similarly, scrambled Aβ_{42} HiLyte 555 Aβ_{42}, and HiLyte Flour 488 Aβ_{42} were prepared (AnaSpec).

Preparing Dispersed SWCNTs.

To prepare ABCNTs we used a selective displacement mechanism, similar to previous displacement- mediated derivatizations of carbon nanotubes.[62,106] We prepared HiPCO-sodium deoxycholate (SDC) wrapped nanotubes. SWCNTs 1 mg Unidym HiPCO (high-pressure carbon monoxide SWCNTs) was added to 1% sodium deoxycholate (SDC) in 1 mL of PBS buffer, and the mixture was probe sonicated (3 mm probe, 750 W, 20 kHz, 40% Amplitude, SONICS VibraCell) at 4 °C for 30 min.

The solution was centrifuged (SORVALL Discovery 90SE, HITACHI) at 250000g for 30 min at 4 °C to remove unsuspended nanotubes and carbon impurities. After centrifugation, 80% of the supernatant was collected and stored at 4 °C until further use. To allow selective transfer of Aβ_{42} to nanotube surface freshly prepared Aβ_{42} prepared in alkaline conditions (see above) was added to SDC wrapped CNTs in a 4:1 weight ratio (Aβ:CNT). Preparation of fluorescently labeled ABCNTs was achieved as described above with the addition of

HiLyte 555 Aβ_{42} (AnaSpec) at 15% of the total Aβ_{42}. To selectively displace the SDC, we used a spin filtration membrane with a low molecular weight cutoff (MWCO) of 500 Da–1 kDa. As the molecular weight of SDC is below the membrane MWCO, at 400 Da, while Aβ_{42} is much higher at 4.5 kDa. Nanotube and protein were transferred to a small volume dialysis device with a 500 Da–1 kD molecular weight cutoff (Spectrum), in a 10 mM NaOH bath (×50 volume). The solution was mixed at 180 rpm for 48 h, with one replacement of bath solution. Then the CNT solution was removed carefully and placed in a small volume dialysis device with a 1000kD molecular weight cutoff (Spectrum), to remove access Aβ_{42}. The bath solution was replaced 3 times every 2 h. ABCNT were removed and characterized by ultraviolet–visible–near-infrared (UV–vis–nIR) absorbance and fluorescence spectroscopies. Absorption and fluorescence spectra were compared to those from precursor SDC-suspended SWCNTs. The concentration was calculated using the extinction coefficient, $\text{Abs}_{632} = 0.036l\ \text{mg}^{-31}\ \text{cm}^{-1}$; where l is the path length. Sensor stocks were kept in 4 °C in NaOH 10 mM solution until use. Ultrapure water (18.2 mΩ) was used for all aqueous solutions.

Preparation of DNA wrapped CNTs was conducted with 2 mg DNA sequence in the place of SDC, according to our previous methods.[107]

Preparation of Oligomers and Fibers.

Conformation-specific Aβ_{42} was prepared according to previously described protocols.[75] Briefly, HFIP treated and dried stocks were dissolved in dimethyl sulfoxide (DMSO) to 5 mM, vortexed, and sonicated in a bath sonicator. This stock was used for unaggregated, oligomeric Aβ, and fibrillar Aβ. Unaggregated Aβ_{42} was immediately diluted in ice-cold Ultrapure water (18.2 mΩ) to 100 μM. Oligomeric Aβ_{42} was prepared by adding cold phenol-free F-12 cell culture media, to a final concentration of 100 mM Aβ_{42}, the solution was then vortexed, and incubated at 4 °C for 24 h. Fibrillar Aβ_{42} was prepared by adding 10 mL of HCl to a final concentration of 100 mM Aβ_{42}, vortexed, and incubated at 37 °C for 24 h. Corresponding vehicle stocks (1% DMSO) were incubated simultaneously. Stocks were diluted in cold Dulbecco's phosphate-buffered saline DPBS (no calcium no magnesium) to a final concentration of 10 μM for fluorescence spectroscopy measurements. Samples for AFM were further diluted ×10 and ×100 for optimal imaging.

Near-Infrared Fluorescence Spectroscopy of Single-Walled Carbon Nanotubes in Solution.

Near-infrared fluorescence microscopy was used to measure the photoluminescence emission from the nanotube sensor, as described previously.[40,67] For solution measurements, spectra were acquired using a home-built near-infrared fluorescence spectroscopy apparatus consisting of 730 nm laser source, inverted microscope, and InGaAs NIR detector. An HL-3-CAL-EXT halogen calibration light source (Ocean Optics) was used to correct for wavelength-dependent features in the emission intensity arising from the spectrometer, detector, and other optics. A Hg/Ne pencil-style calibration lamp (Newport) was used to calibrate the spectrometer wavelength. A continuous wave 730 nm diode laser with an output power of 2W in was injected into a multimode fiber to produce the excitation source for fluorescence experiments. The light path was shaped and fed into the back of an inverted IX-71 microscope (Olympus), where it passed through a 20× NIR objective (Olympus) and

illuminated the sensor samples in a 96-well plate. Emission from the sensor was collected through the 20× objective and passed through a dichroic mirror (875 nm cutoff, Semrock). The light was f/# matched to the spectrometer using several lenses and injected into a Shamrock 303i spectrograph (Andor, Oxford Instruments) with a slit width of 100 μm, which dispersed the emission using 86 g/mm grating with 1.35 μm blaze wavelength. The spectral range was 723–1694 nm with a resolution of 1.89 nm. The light was collected by an iDus 1.7 μm InGaAs (Andor, Oxford Instruments). To acquire photoluminescence emission from all CNT chirality's the 730 nm laser source was replaced with a supercontinuum white-light laser source (SuperK EXTREME, NKT Photonics) with a VARIA variable bandpass filter. The excitation wavelength was tuned from 500–825 nm, with a bandwidth of 20 nm centered at 575 nm.

Typical sensor experiments were conducted with freshly prepared ABCNT diluted with DPBS to 0.1 μg/mL in a 96-well plate. Experiment wells contained freshly prepared Aβ, and to match solvent properties 10 mM NaOH, or DMSO, was proportionally added to control wells. Hydrochloric acid (HCl) was added when necessary to neutralize the pH conditions. Background subtraction was conducted using a well filled with DPBS. For analyte screening, bovine serum albumin (Sigma-Aldrich), sphingomyelin (Avanti Polar lipids), α-synuclein (AnaSpec), and scrambled Aβ_{42} (AnaSpec) were diluted in appropriate solutions, corresponding to solution conditions in ABCNT wells. For measurements in serum, we used fetal bovine serum at 10% or 33% final concentrations in PBS. During the measurements, the excitation wavelength remained at 730 nm, close to the resonant excitation maximum of the Aβ-wrapped (9,4) and (8,6) nanotube species. Following the acquisition, the data were processed with custom code written in MATLAB to subtract background and correct for nonuniformities in the excitation profile. Corrected and smoothed data were used to fit with Lorentzian functions to extract center wavelength, intensity, and full width at half-maximum (FWHM). Data for dose–response curves were fitted with one-phase decay in GraphPad Prism ($R^2 > 0.97$). Excitation/emission plots, also dubbed PL plots, were compiled using the supercontinuum laser for excitation. Spectra were acquired between movements of the VARIA bandpass filter in 3 nm steps from 500 to 827 nm.

Zeta-Potential Measurements.—Zeta-potential measurements were performed with a Zetasizer Nano S (Malvern Instruments) device and evaluated with Zetasizer software. Two Different stocks ABCNTs and SDC-CNTs were diluted in PBS and measured in triplicates.

Thioflavin T (ThT) Assay.

ThT stock was freshly prepared for each experiment. ThT (Sigma) was dissolved in PBS buffer and filtered through a 0.2 μm syringe filter. The concentration of ThT was determined using $Abs_{412} = 36$ mM^{-1} cm^{-1}, where l is the path length[108] and brought to 25 μM in a 96-well flat clear bottom black plate (Corning) freshly prepared Aβ_{42} and ABCNTs were diluted to a final concentration of 10 μM and 0.1 μg/mL, respectively, in ThT (final concentration 22 μM). The plate was sealed with sealing tape for optical assays (bio rad). Plates were shaken (654 rpm) for 30 s, and the fluorescent signal of each well was then immediately measured by a fluorescent plate reader (Infinite M1000 Pro, Tecan), using λ_{ex} of 450 nm and λ_{em} of 485 nm. Hourly measurements were taken with the same parameters

for 17 h. The fluorescent signal was subtracted from background wells containing ThT alone, and the signal was normalized to time zero. Smoothed data of three technical replicates are shown. Data were fit to a nonlinear agonist vs response model ($R^2 > 0.98$) in Graphpad Prism (V 7.04). For measuring ABCNT effect on preformed fibrils, fibrillary $A\beta_{42}$ [10 μM] was incubated with ABCNTs [0.1 μg/mL] for 1 h at rt, and ThT fluorescence measurements were taken as described above.

Fluorescence Quenching by ABCNT.

HiLyte 555 $A\beta_{42}$ and ABCNT were prepared as described. HiLyte 555 $A\beta_{42}$ at increasing concentration was added to ABCNT (final concentration 1 μg/mL) in PBS in a 96-well flat clear bottom black plate (Corning), and fluorescence was immediately measured (Infinite M1000 Pro, Tecan) with λex 555 nm and λem 580 nm. Background fluorescence was corrected with wells containing ABCNT in PBS, and the results are shown for one of the experiments carried out in triplicate.

AFM.

Atomic Force Microscopy.—A 20 μL aqueous solution of SWCNTs (0.01 μg/mL, in filtered Ultrapure water (18.2 mΩ) was dropped onto a pretreated MICA with 3-aminopropyltriethoxysilane (APTES) (Pelco Mica Disc, V1, Ted Pella) and allowed to stand for 45s. The mica surface was rinsed with deionized water two times to remove unbound carbon nanotubes and air-dried at room temperature before AFM imaging. AFM images were collected using an Asylum MFD-3D-BIO in ac mode using AC240TS and AC160TS tips (Asylum Research). The typical scan size was 1–5 μm, and the scan rate was 0.5–1 Hz. The images were processed with Gwyddion 2.47 software. A minimum of 40 nanotubes per group was analyzed for height analysis derived from 1×1 μm^2 images.

Atomic Force Microscopy: Young's Modulus Measurements.—Young's modulus measurements were performed on the same AP-mica slides containing Argon-dried SWCNTs. A spherical probe with a 600 nm SiO2 glass bead (Novascan) was used in this experiment, and the nominal spring constant is 1 N/m. The cantilever spring constant was calibrated using the thermal noise method. The scan size is 1×1 μm^2, and the force point and line are 20×20. The rate of a single approach/withdraw cycle was set to 0.7 Hz, and the force–distance was 1 μm. Force curves in each map were fitted according to the Hertz model using the routine implemented in the MFP 3D AFM to obtain elastic modulus maps (Igor Pro, Wavemetrics) ($\nu_{tip} = 0.5$, $E_{tip} = 68$ GPa, $\nu_{sample} = 0.5$).

Cell Cultures.

Neuro-2a (N2A) Mouse Neuroblastoma Cells.—Mouse neuroblastoma N2a cells stably expressing APP695 (N2a-APP) and/or N2a (n2a WT) were received from Yueming Li lab. Cells were grown Dulbecco's Modified Eagle Medium with high glucose (Thermo Fisher Scientific) supplemented with 10% heat-inactivated fetal bovine serum (HI-FBS), 2 mM Glutamx (Thermo Fisher Scientific), and 1% penicillin-streptomycin (10000 U/mL) (Thermo Fisher Scientific) and maintained 37 °C with 5% CO$_2$ until 70–80% confluency. Cells were seeded at 100,000 cells/mL in 24 well plates (Corning) for media extraction, and media was replaced with Opti-Mem (Thermo Fisher Scientific). After 48 h, the media

was collected from each well and stored at −20 °C until use. Extracted media was then transferred to a 96-well clear bottom well plate (Corning), and freshly prepared ABCNT was added [1 μg/mL]. Data was collected in three technical replicates for each experiment well following 24 h incubation. The center wavelength was derived for each data point and subtracted from Opti-Mem control samples as a baseline.

For imaging experiments, 100000 cells/mL in 24 well plates were plated in a 35 mm^2 glass bottom plate (MetTek) for hyperspectral imaging. Following 24 h, cells were pulsed with ABCNT [1 μg/mL] in DPBS for 30 min, then cells were washed, and fresh media was added. Cells were imaged in hyperspectral microscope following 24 h incubation, with the acquisition of at least 9 hyperspectral cubes per plate. Results are shown of average of three biological replicates.

Cell Titer Glow.—100 μL Cells were plated at WT and APP N2a cells at 100000 cells/mL Opaque white clear-bottom 96-well culture plates (Corning). After overnight freshly prepared Aβ-CNTs were added to the cells in 0.1, 0.2, 0.5, 0.7, and 1 μg/mL in PBS. Cells were loaded with the ABCNT sensor for 30 min, then washed, and media was replenished. For assessing the recovery effect from Aβ toxicity, N2a WT cells loaded 1 μg/mL ABCNT were incubated with freshly prepared Aβ_{42} in a final concentration of 10 μM. Corresponding vehicle (10 mM NaOH) was added in control wells. Additional wells containing media alone were kept for background subtraction. Following 72 h of incubation cell viability was assessed with Luminescent Cell Viability Assay (Promega), as detailed by the manufacturer's instructions. Briefly, CellTiter-Glo Reagent was freshly mixed, and 30 μL was added to experiment wells. Cells were equilibrated at room temperature for 10 min, and the emitted luminescence was recorded with (Infinite M1000 Pro, Tecan). Background luminescence was corrected, and results are shown of one experiment carried in triplicates, out of a series of three showing similar trends.

SH-SY5Y Culture and Differentiation.

Human neuroblastoma cells (SH-SY5Y) were grown in Eagle's Minimum Essential Medium (EMEM) (Thermo Fisher Scientific), including 15% heat-inactivated fetal bovine serum (HI-FBS), 2 mM Glutamx (Thermo Fisher Scientific), and 1% penicillin-streptomycin (10,000 U/mL) (Thermo Fisher Scientific) and maintained 37 °C with 5% CO_2 until 70–80% confluency. Cells were differentiated according to the protocol[78,109] and selected against epithelial cells by gradual serum-starvation, with the introduction of extracellular matrix proteins and neurotrophic factors. Briefly, undifferentiated SH-SY5Y cells were platted in 50000 cells/mL 35 mm^2 glass-bottom plates (MatTek). For 7 days, media was replaced every other day with an addition of low serum media (2.5% HI-FBS) and freshly added retinoic acid (RA) [10 μM] (Sigma-Aldrich). On day 7 cells were split onto new plates, and sequential addition of low serum (1% HI-FBS) with fresh RA were added. On day 10, cells were split onto prepared 35 mm^2 glass-bottom plates (MetTeck) precoated with Matrigel (Corning). SH-SY5Y were continuedly differentiated with a Neurobasal media (Life Technologies-Gibco) with 2 mM Glutamx (Thermo Fisher Scientific), 1% penicillin-streptomycin (10,000 U/mL K1), (Thermo Fisher scientific), B-27 (Gibco), 1 M KCl, dibutyl cyclic-AMP (Sigma), and freshly added RA [10 μM], with two sequential exchanges

of media every 3 days. Differentiated cells were loaded with ABCNT [1 μg/mL] in DPBS for 30 min, and then cells were washed and freshly prepared Aβ_{42} [1 μM]. Scrambled Aβ_{42} [1 μM] or NaOH (vehicle) was added to the cells in differentiation media without RA. Cells were imaged in hyperspectral microscope following 24 h incubation, with the acquisition of at least nine hyperspectral cubes. Experiments were conducted in three biological replicates.

Hyperspectral Microscopy and Analysis.

Hyperspectral microscopy was performed as described previously.[107] A continuous-wave 730 nm diode laser with an output power of 2W was injected into a multimode fiber to provide an excitation source for experiments. Homogenous illumination over the field of view was assured by passing the excitation beam through a custom beam shaping module to produce a top-hat intensity profile with a maximum of 20% variation on the surface of the sample. The laser was reflected into an Olympus IX-71 inverted microscope (with internal optics modified for near-infrared transmission) equipped with a 50× air objective or 100× (UAPON100XOTIRF, NA = 1.49) oil objective (Olympus, USA) via a long pass dichroic mirror with a cut-on wavelength of 880 nm. The spatially defined near-infrared emission was collected from the sample through a volume Bragg grating (VBG) to resolved emission wavelength. Following its passage through the VBG, a specific wavelength component of emitted polychromatic light was diffracted, while all other wavelengths were transmitted through the grating. The diffracted component then passed through the VBG a second time resulting in a monochromatic beam which was collected by a 256 × 320 pixel InGaAs array (Photon Etc.). Finally, the filtered image produced on the InGaAs camera was composed of a series of vertical lines, each with a specific wavelength. The reconstruction of a spatially rectified image stack was performed using cubic interpolation on every pixel for each monochromatic image, according to the wavelength calibration parameters. The rectification produced a hyperspectral "cube" of images of the same spatial region exhibiting distinct spectral.

Fluorescence Microscopy of Live Cells.

Standard fluorescence imaging in the UV–vis emission range was performed on the hyperspectral microscope by using an XCite Series 120Q lamp as the light source and a QiClick CCD camera (QImaging) directly attached to a c-mount on a separate port of the microscope. Fluorescence filter sets from Chroma Technology and Semrock were used. Back-to-back images were acquired with the near IR hyperspectral microscope and live-imaging of fluorescently labeled Aβ-CNTs in THP-1 cells was performed on a Zeiss LSM 880.

Analysis and Processing of Hyperspectral Data.—Acquired hyperspectral data was saved as 16-bit arrays (320 × 256 × Y), where the first two coordinates represent the spatial location of a pixel and the last coordinate its position in wavelength space (1100–1250 nm). Following Hyperspectral acquisition, the data was processed with custom code written in MATLAB to identify individual pixel center wavelengths. A peak finding algorithm was used to determine the intensity range for a given pixel, i.e., range = (intensity_maximum– intensity_minimum). Data points were designated as peaks if their intensity was range/4 greater than the intensity of adjacent pixels. Pixels that did not meet this threshold (primarily

due to low signal above background) were removed from the data sets. The remaining pixels were fit with a Lorentzian function. The Center wavelengths for single pixels were plotted as a histogram (example S13d), and he peak wavelength was derived for each condition and biological replicate. The results are shown as the average of biological replicate ± SE.

Alternatively, an individual region of interest (ROI) analysis was performed. Manual ROIs were selected from hyperspectral "cube" data" in ImageJ software. Spectra were extracted for each ROI, interpolated and smoothed and finally, a peak finding algorithm was applied to obtain center wavelength and FWHM. Outliers were removed based on FWHM (90%, excluding lower 5% and upper 95%) to remove possible aggregated CNTs from ROIs or background noise. The individual center wavelengths for ROIs were plotted and averaged.

THP-1 Cells.

Human monocyte-like THP-1 cells were grown in RPMI 1640 medium (Thermo Fisher Scientific), including 10% heat-inactivated fetal bovine serum (HI-FBS), 2 mM Glutamx (Thermo Fisher Scientific), and 1% penicillin-streptomycin (10000 U/mL) (Thermo Fisher Scientific) and maintained 37 °C with 5% CO_2. For experiments, cells were seeded in a 96-well clear bottom plate (corning). THP-1 activation was achieved by adding 100 ng/mL Phorbol 12-myristate 13-acetate (PMA) (Fisher Bioreagents) in the media for 24 h. Cells were then loaded with ABCNT [1 μg/mL] in DPBS for 30 min and washed, and freshly prepared Aβ_{42} [1 μM] or NaOH (vehicle) was added. Data acquisition was at 0 time points, 4 and 24 h following Aβ addition.

Cells were fixed in 4% PFA, and the immunofluorescence detections of B-amyloid ab slides were performed at Molecular Cytology Core Facility of Memorial Sloan Kettering Cancer Center using Discovery Ultra processor (Ventana Medical Systems. Roche- AZ). A mouse monoclonal IgG1 anti- B-amyloid (clone 6E10) antibody (Biolegend, cat no. 803004) was used in 5 μg/mL concentration. The incubation with the primary antibody was done for 5 h, followed by Rb antimouse IgG1 (Abcam cat#ab133469) for 32 and 60 min incubation with biotinylated goat antirabbit IgG (Vector laboratories, cat. no. PK6101) in 5.75 μg/mL. Blocker D, Streptavidin-HRP, and TSA Alexa488 (Life Tech, cat. no. B40932) were used for 16 min.

All slides were counterstained in 5 μg/mL DAPI [dihydrochloride-(2-(4-Amidinophenyl)-6-indolecarbamidine dihydrochloride] (Sigma D9542), for 5 min at room temperature, mounted with antifade mounting medium Mowiol [Mowiol 4–88 (CALBIOCHEM code: 475904)], and covered by a coverslip.

Near-Infrared Fluorescence Spectroscopy of Single-Walled Carbon Nanotubes from Cells.

Before the acquisition, the fluorescence spectroscopy apparatus was adjusted to allow maximum signal collection from cells by adjusting the z position of the objective. Nanotube photoluminescence was collected from 96-well plate-containing cells. Background subtraction was conducted using a media-filled well. During the measurements, the excitation wavelength remained at 730 nm, close to the resonant excitation maximum of the Aβ-wrapped (9,4) and (8,6) nanotube species. Following the acquisition, the data were processed with custom code written in MATLAB to subtract background noise and correct

for nonuniformities in the excitation profile. Corrected and smoothed data were used to fit with Lorentzian functions to extract center wavelength, intensity, and full width at half-maximum (FWHM).

Animals Studies.

All animal studies were approved by and carried out by the Memorial Sloan Kettering Cancer Center Institutional Animal Care and Use Committee. Male B6.Cg-Tg (APPSwFlLon, PSEN1*M146L*L286 V)6799Vas/Mmjax (5XFAD) and WT mice were bred in the lab of Li laboratory (Memorial Sloan Kettering) and were graciously provided at 4 months and 8 months of age for stereotaxic injections. All control and experimental mice were age- matched and housed in identical environments

Stereotaxic Injection of ABCNT.

Each mouse was injected intraperitoneally with a mixture of mixture ketamine (50 mg/kg) + dexmedetomidine (0.5 mg/kg) to produce deep anesthesia. The mouse was mounted in a stereotactic frame (Harvard Apparatus 75–1820) and its head shaved. A midline sagittal incision was made to expose the skull. Cotton swabs were used to remove the periosteum and clean the skull surface. Coordinates were identified from bregma, and a burr hole was drilled with a micro drill (cellpoint scientific, 0.8 mm wide). We used the following coordinates to target the dentate gyrus of the hippocampus: anteroposterior (AP) –2.0 mm, mediolateral (ML) +1.5 mm, dorsoventral (DV) –2.0 mm, from bregma. After a pause of at least 2 min for pressure equalization, the injection was performed manually at an approximate rate of 0.4 μL per minute. Afterward, the syringe was left in place for an additional 3 min, then withdrawn over 2 min or more. Once injections were complete, the scalp was sutured and the mouse was kept under a warming lamp until recovered from the anesthesia, then returned to standard housing. Near-infrared in vivo spectroscopy was acquired 24 h following injection, $n = 4$ mice in each group (1 mouse died and was excluded from results).

Near-Infrared In Vivo Spectroscopy.—Noninvasive in vivo spectra were taken using a custom-built reflectance probe-based spectroscopy system. Excitation light was provided by injecting a continuous wave 730 nm diode laser (Frankfurt) into a bifurcated fiber optic reflection probe bundle (Thorlabs). The sample leg of the bundle included one 200 μm, 0.22 NA fiber optic cable for sample excitation located in the center of six 200 μm, 0.22 NA fiber optic cables for collection of the emitted light. Excitation power at the sample was ~590 mW with an ~1 cm circle being illuminated. Long pass filters were used to filter emission light below 1050 nm, and emission light was focused through a 410 μm slit into a Czerny-Turner spectrograph with 303 mm focal length (Shamrock 303i, Andor). Emission light was dispersed by an 85 g/mm grating with 1350 blaze wavelength and collected by an iDus InGaAs camera (Andor). For in vivo spectroscopy, mice were anesthetized with 2% isoflurane prior to data collection. An exposure time of 1or 3 s was used for all in vivo data acquisition, with 1–3 optical measurements per mouse, to account for instrument signal-to-noise. Additional ex-vivo data was acquired per mice following animal sacrifice. Following acquisition data was processed to apply spectral corrections for nonlinearity of the InGaAs detector response, background subtraction, and baseline subtraction. Center

wavelengths were determined by fitting processed spectra to a Lorentzian function. Results were threshold based on R^2 and FWHM values. Data is shown as average of repeated measurements. Results are shown of in vivo or ex vivo data obtained from biological replicates.

Immunofluorescence Staining.

WT and 5XFAD mice were anesthetized with a single dose of ketamine/xylazine (100 mg/kg/5.0 mg/kg) and transcardially perfused with 50 mL of PBS followed by 50 mL of 4% paraformaldehyde (PFA). Brains were removed and post fixed in 4% PFA overnight at 4 °C and then processed for paraffin embedding with tissue processor (Leica Biosystems, ASP6025). Paraffin-embedded perfused brains were sectioned sagittally at 10 μm and mounted on slides. Slides were washed twice in 100% Xylene 100% for 3 min, followed by 3 min in xylene 1:1 100% EtOH, 3 min in 100% EtOH, 3 min in 95% EtOH, 3 min in 70% EtOH, 3 min in 50% EtOH, 3 min in H$_2$0 and then boiled in citrate buffer, pH 6.0 for 15 min. Slides were left in citrate buffer to cool to room temperature and then washed 3× in PBS. Slides were incubated in PBST (PBS + 0.05% Triton X-100) for 20 min at room temperature followed by blocking buffer (PBST + 10% Donkey Serum) for 40 min at room temperature. Slides were then incubated in anti-Iba1 (Abcam, cat. no. ab178847, 1:200), antiNeuN (Abcam cat. no. ab 104224, 1:200), or 6e10 (Biolegend, cat. no. 803004, anti-β-Amyloid, 1–16 Antibody, 1:500), cleaved caspase-3 antibody (cell signaling no. 9661, 1:200), or anti-p53 (Abcam cat. no. ab183544, 1:250) in blocking buffer overnight at 4 °C. Sections were then washed three times in PBST for 5 min. Slides were incubated in 1:10000 Donkey anti-Mouse IgG Alexa Fluor 568 (A10037) and 1:10000 Donkey anti-Rabbit IgG Alexa Fluor 488 (A21206) in 50% blocking buffer/50% PBS for 1 h at room temperature and then washed 3 times with PBST. Slides were incubated in Dapi for 10 min and then washed 3 times in PBS and mounted with Fluoromount-G Mounting Medium (00–4958-02). Slides were dried at room temperature while protected from light. H&E staining was performed at the Molecular Cytology Core Facility at Memorial Sloan Kettering Cancer Center. Back-to-back images were acquired with the near IR hyperspectral microscope and a digital slide scanner.

Statistics.

Statistical analysis was performed with GraphPad Prism version 7.04. All data met the assumptions of the statistical tests performed. To account for the testing of multiple hypotheses, one-way ANOVAs were performed with Dunnet's, Tukey's, or Sidak's post-tests when appropriate. To account for time- measurements and test multiple hypotheses two-way ANOVA were preformed with Sidak's post-tests.

Supplementary Material

Refer to Web version on PubMed Central for supplementary material.

ACKNOWLEDGMENTS

Core Facility (MCCF) at Memorial Sloan Kettering Cancer Center for their expert help and support in AFM imaging, live-cell confocal microscopy, and tissue sectioning and preparation. We especially acknowledge Biran Wang, Afsar Barlas, Ning Fan, Yevgeniy Romin, and Eric Chan.

REFERENCES

(1). T. V.T. V.Alzheimer's Disease International. World Alzheimer Report 2019: Attitudes to dementia; Alzheimer's Disease International: London, 2019). www.daviddesigns.co.uk (accessed 2022-03-30).

(2). GBD 2016 Dementia Collaborators. Global, regional, and national burden of Alzheimer's disease and other dementias, 1990–2016: a systematic analysis for the Global Burden of Disease Study 2016. Lancet. Neurol. 2019, 18, 88–106. [PubMed: 30497964]

(3). Mehta D; Jackson R; Paul G; Shi J; Sabbagh M Why do trials for Alzheimer's disease drugs keep failing? A discontinued drug perspective for 2010–2015. Expert Opin. Investig. Drugs 2017, 26, 735–739.

(4). Viña J; Sanz-Ros J Alzheimer's disease: Only prevention makes sense. Eur. J. Clin. Invest. 2018, 48, No. e13005.

(5). Jack CR; Holtzman DM Biomarker Modeling of Alzheimer's Disease. Neuron 2013, 80, 1347–1358. [PubMed: 24360540]

(6). Leuzy A; Heurling K; Ashton NJ; Schöll M; Zimmer ER In vivo detection of alzheimer's disease. Yale Journal of Biology and Medicine 2018, 91, 291–300. [PubMed: 30258316]

(7). Jack CR; et al. NIA-AA Research Framework: Toward a biological definition of Alzheimer's disease. Alzheimer's and Dementia 2018, 14, 535–562.

(8). Sanabria-Castro A; Alvarado-Echeverría I; Monge-Bonilla C Molecular Pathogenesis of Alzheimer's Disease: An Update. Ann. Neurosci. 2017, 24, 46–54. [PubMed: 28588356]

(9). Selkoe DJ; Hardy J The amyloid hypothesis of Alzheimer's disease at 25 years. EMBO Mol. Med 2016, 8, 595–608. [PubMed: 27025652]

(10). El-Agnaf OMA; Mahil DS; Patel BP; Austen BM Oligomerization and toxicity of β-amyloid-42 implicated in Alzheimer's disease. Biochem. Biophys. Res. Commun. 2000, 273, 1003–1007. [PubMed: 10891362]

(11). Bayer TA; Wirths O Intracellular accumulation of amyloid – beta - A predictor for synaptic dysfunction and neuron loss in Alzheimer's disease. Front. Aging Neurosci. 2010, 2, 8. [PubMed: 20552046]

(12). LaFerla FM; Green KN; Oddo S Intracellular amyloid-β in Alzheimer's disease. Nat. Rev. Neurosci. 2007, 8, 499–509. [PubMed: 17551515]

(13). Takahashi RH; Nagao T; Gouras GK Plaque formation and the intraneuronal accumulation of β-amyloid in Alzheimer's disease. Pathology International 2017, 67, 185–193. [PubMed: 28261941]

(14). Oakley H; et al. Intraneuronal β-amyloid aggregates, neurodegeneration, and neuron loss in transgenic mice with five familial Alzheimer's disease mutations: Potential factors in amyloid plaque formation. J. Neurosci. 2006, 26, 10129–10140. [PubMed: 17021169]

(15). Youmans KL; et al. Intraneuronal Aβ detection in 5xFAD mice by a new Aβ-specific antibody. Mol. Neurodegener. 2012, 7, 8. [PubMed: 22423893]

(16). Gouras GK; Almeida CG; Takahashi RH Intraneuronal Aβ accumulation and origin of plaques in Alzheimer's disease. Neurobiology of Aging 2005, 26, 1235–1244. [PubMed: 16023263]

(17). Gold M; El Khoury J β-amyloid, microglia, and the inflammasome in Alzheimer's disease. Seminars in Immunopathology 2015, 37, 607–611. [PubMed: 26251237]

(18). Ahmad J; et al. Nanotechnology Based Theranostic Approaches in Alzheimer's Disease Management: Current Status and Future Perspective. Curr. Alzheimer Res. 2017, 14, 1164. [PubMed: 28482786]

(19). Ling D; Magallanes M; Salvaterra PM Accumulation of amyloid-like Aβ1–42 in AEL (autophagy-endosomal-lysosomal) vesicles: Potential implications for plaque biogenesis. ASN Neuro 2014, 6, 95–109.

(20). Nixon RA The role of autophagy in neurodegenerative disease. Nature Medicine 2013, 19, 983–997.

(21). Ries M; Sastre M Mechanisms of Aβ clearance and degradation by glial cells. Frontiers in Aging Neuroscience 2016, 8, 160. [PubMed: 27458370]

(22). Hickman SE; Allison EK; El Khoury J Microglial dysfunction and defective β-amyloid clearance pathways in aging alzheimer's disease mice. J. Neurosci. 2008, 28, 8354–8360. [PubMed: 18701698]

(23). Schmidt SD; Mazzella MJ; Nixon RA; Mathews PM Aβ measurement by enzyme-linked immunosorbent assay. Methods Mol. Biol 2012, 849, 849.

(24). Portelius E; et al. Mass spectrometric characterization of brain amyloid beta isoform signatures in familial and sporadic Alzheimer's disease. Acta Neuropathol. 2010, 5, 120.

(25). Adlard PA; et al. A review of β-amyloid neuroimaging in Alzheimer's disease. Front. Neurosci. 2014, 8, 327. [PubMed: 25400539]

(26). Yang J; et al. Development of Near-Infrared Fluorescent Probes for Use in Alzheimer's Disease Diagnosis. Bioconjugate Chem. 2020, 31, 2–15.

(27). Zhang X; et al. Near-infrared fluorescence molecular imaging of amyloid beta species and monitoring therapy in animal models of Alzheimer's disease. Proc. Natl. Acad. Sci. U. S. A. 2015, 112, 9734–9739. [PubMed: 26199414]

(28). Ni R; et al. In-vitro and in-vivo characterization of CRANAD-2 for multi-spectral optoacoustic tomography and fluorescence imaging of amyloid-beta deposits in Alzheimer mice. Photoacoustics 2021, 23, 100285. [PubMed: 34354924]

(29). Lu M; et al. Structural progression of amyloid- Arctic mutant aggregation in cells revealed by multiparametric imaging. J. Biol. Chem. 2019, 294, 1478–1487. [PubMed: 30504224]

(30). Li T; et al. Camelid single-domain antibodies: A versatile tool for in vivo imaging of extracellular and intracellular brain targets. J. Controlled Release 2016, 243, 1–10.

(31). Zheng M; et al. DNA-assisted dispersion and separation of carbon nanotubes. Nat. Mater. 2003, 2, 338–342. [PubMed: 12692536]

(32). Ge C; et al. Binding of blood proteins to carbon nanotubes reduces cytotoxicity. Proc. Natl. Acad. Sci. U. S. A. 2011, 108, 16968–16973. [PubMed: 21969544]

(33). Edri E; Regev O pH effects on BSA-dispersed carbon nanotubes studied by spectroscopy-enhanced composition evaluation techniques. Anal. Chem. 2008, 80, 4049–4054. [PubMed: 18459735]

(34). Nepal D; Geckeler KE pH-Sensitive Dispersion and Debundling of Single-Walled Carbon Nanotubes: Lysozyme as a Tool. Small 2006, 2, 406–412. [PubMed: 17193060]

(35). Nepal D; Geckeler KE Proteins and carbon nanotubes: Close encounter in water. Small 2007, 3, 1259–1265. [PubMed: 17492743]

(36). Zhang J; et al. Molecular recognition using corona phase complexes made of synthetic polymers adsorbed on carbon nanotubes. Nat. Nanotechnol. 2013, 8, 959–968. [PubMed: 24270641]

(37). Boghossian AA; et al. Near-Infrared Fluorescent Sensors based on Single-Walled Carbon Nanotubes for Life Sciences Applications. ChemSusChem 2011, 4, 848–863. [PubMed: 21751417]

(38). Williams RM; et al. Noninvasive ovarian cancer biomarker detection via an optical nanosensor implant. Sci. Adv. 2018, 4, No. eaaq1090.

(39). Harvey JD; et al. A carbon nanotube reporter of microRNA hybridization events in vivo. Nat. Biomed. Eng. 2017, 1, 0041. [PubMed: 28845337]

(40). Jena PV; et al. A Carbon Nanotube Optical Reporter Maps Endolysosomal Lipid Flux. ACS Nano 2017, 11, 10689–10703. [PubMed: 28898055]

(41). Kruss S; et al. Neurotransmitter Detection Using Corona Phase Molecular Recognition on Fluorescent Single-Walled Carbon Nanotube Sensors. J. Am. Chem. Soc. 2014, 136, 713–724. [PubMed: 24354436]

(42). Beyene AG; et al. Imaging striatal dopamine release using a nongenetically encoded near infrared fluorescent catecholamine nanosensor. Sci. Adv. 2019, 5, 5.

(43). Godin AG; et al. Single-nanotube tracking reveals the nanoscale organization of the extracellular space in the live brain. Nat. Nanotechnol. 2016 123 2017, 12, 238–243. [PubMed: 27870840]

(44). Lee HJ; et al. Amine-modified single-walled carbon nanotubes protect neurons from injury in a rat stroke model. Nat. Nanotechnol. 2011, 6, 121–125. [PubMed: 21278749]

(45). Mohajeri M; Behnam B; Barreto GE; Sahebkar A Carbon nanomaterials and amyloid-beta interactions: potentials for the detection and treatment of Alzheimer's disease? Pharmacol. Res. 2019, 143, 186–203. [PubMed: 30943430]

(46). Kim JE; Lee M Fullerene inhibits β-amyloid peptide aggregation. Biochem. Biophys. Res. Commun. 2003, 303, 576–579. [PubMed: 12659858]

(47). Xie L; et al. The molecular mechanism of fullerene-inhibited aggregation of Alzheimer's β-amyloid peptide fragment. Nanoscale 2014, 6, 9752–9762. [PubMed: 25004796]

(48). Li H; Luo Y; Derreumaux P; Wei G Carbon Nanotube Inhibits the Formation of β-Sheet-Rich Oligomers of the Alzheimer's Amyloid-β(16–22) Peptide. Biophys. J. 2011, 101, 2267–2276. [PubMed: 22067167]

(49). Fu Z; Luo Y; Derreumaux P; Wei G Induced β-barrel formation of the Alzheimer's Aβ25–35 oligomers on carbon nanotube surfaces: Implication for amyloid fibril inhibition. Biophys. J. 2009, 97, 1795–1803. [PubMed: 19751686]

(50). Luo J; et al. The Aβ peptide forms non-amyloid fibrils in the presence of carbon nanotubes. Nanoscale 2014, 6, 6720–6726. [PubMed: 24820873]

(51). Liu F; Wang W; Sang J; Jia L; Lu F Hydroxylated Single-Walled Carbon Nanotubes Inhibit Aβ 42 Fibrillogenesis, Disaggregate Mature Fibrils, and Protect against Aβ 42 -Induced Cytotoxicity. ACS Chem. Neurosci. 2019, 10, 588–598. [PubMed: 30335950]

(52). Jana AK; Sengupta N Adsorption mechanism and collapse propensities of the full-length, monomeric Aβ 1–42 on the surface of a single-walled carbon nanotube: A molecular dynamics simulation study. Biophys. J. 2012, 102, 1889–1896. [PubMed: 22768945]

(53). Zhang N; et al. Tuning the structure of monomeric amyloid beta peptide by curvature of carbon nanotubes. Carbon N. Y. 2019, 153, 717–724.

(54). Meisl G; et al. Differences in nucleation behavior underlie the contrasting aggregation kinetics of the Aβ40 and Aβ42 peptides. Proc. Natl. Acad. Sci. U. S. A. 2014, 111, 9384–9389. [PubMed: 24938782]

(55). Zheng M; et al. DNA-assisted dispersion and separation of carbon nanotubes. Nat. Mater. 2003, 2, 338–342. [PubMed: 12692536]

(56). Yudasaka M; et al. Diameter Enlargement of HiPco Single-Wall Carbon Nanotubes by Heat Treatment. Nano Lett. 2001, 1, 487–489.

(57). Nirmalraj PN; et al. Complete aggregation pathway of amyloid β (1–40) and (1–42) resolved on an atomically clean interface. Sci. Adv. 2020, 6, No. eaaz6014.

(58). Mastrangelo IA; et al. High-resolution atomic force microscopy of soluble Aβ42 oligomers. J. Mol. Biol. 2006, 358, 106–119. [PubMed: 16499926]

(59). Rokadia H, Tung S, Spearot D Experimental characterization of DNA/CNT hybrid structures with atomic force microscope. In 2008 8th IEEE Conference on Nanotechnology, 18–21 Aug , 2018, Arlington, TX; IEEE, 2008; pp 255–258. DOI: 10.1109/NANO.2008.82.

(60). Naumov AV; Ghosh S; Tsyboulski DA; Bachilo SM; Weisman RB Analyzing absorption backgrounds in single-walled carbon nanotube spectra. ACS Nano 2011, 5, 1639–1648. [PubMed: 21341755]

(61). Haggenmueller R; et al. Comparison of the quality of aqueous dispersions of single wall carbon nanotubes using surfactants and biomolecules. Langmuir 2008, 24, 5070–5078. [PubMed: 18442227]

(62). Jena PV; Safaee MM; Heller DA; Roxbury D DNA-Carbon Nanotube Complexation Affinity and Photoluminescence Modulation Are Independent. ACS Appl. Mater. Interfaces 2017, 9, 21397–21405. [PubMed: 28573867]

(63). Jiang D; Rauda I; Han S; Chen S; Zhou F Aggregation pathways of the amyloid β(1 42) peptide depend on its colloidal stability and ordered β-sheet stacking. Langmuir 2012, 28, 12711–12721. [PubMed: 22870885]

(64). Antonucci A; Kupis-Rozmysłowicz J; Boghossian AA Noncovalent Protein and Peptide Functionalization of Single-Walled Carbon Nanotubes for Biodelivery and Optical Sensing Applications. ACS Appl. Mater. Interfaces 2017, 9, 11321–11331. [PubMed: 28299937]

(65). Tokuraku K; Marquardt M; Ikezu T Real-Time Imaging and Quantification of Amyloid-β Peptide Aggregates by Novel Quantum- Dot Nanoprobes. PLoS One 2009, 4, No. e8492.

(66). Richman M; Wilk S; Skirtenko N; Perelman A; Rahimipour S Surface-modified protein microspheres capture amyloid-β and inhibit its aggregation and toxicity. Chem. - A Eur. J 2011, 17, 11171–11177.

(67). Galassi TV; et al. An optical nanoreporter of endolysosomal lipid accumulation reveals enduring effects of diet on hepatic macrophages in vivo. Sci. Transl. Med. 2018, 10, No. eaar2680.

(68). Weisman RB Chapter 5 Optical spectroscopy of single-walled carbon nanotubes. Contemporary Concepts of Condensed Matter Science 2008, 3, 109–133.

(69). Shvartzman-Cohen R; et al. Selective dispersion of single-walled carbon nanotubes in the presence of polymers: The role of molecular and colloidal length scales. J. Am. Chem. Soc. 2004, 126, 14850–14857. [PubMed: 15535711]

(70). Chiu CF; Dementev N; Borguet E Fluorescence quenching of dyes covalently attached to single-walled carbon nanotubes. J. Phys. Chem. A 2011, 115, 9579–9584. [PubMed: 21766814]

(71). Yang R; et al. Carbon nanotube-quenched fluorescent oligonucleotides: Probes that fluoresce upon hybridization. J. Am. Chem. Soc. 2008, 130, 8351–8358. [PubMed: 18528999]

(72). Esbjörner EK; et al. Direct observations of amyloid β Self-assembly in live cells provide insights into differences in the kinetics of Aβ(1–40) and Aβ(1–42) aggregation. Chem. Biol. 2014, 21, 732–742. [PubMed: 24856820]

(73). Quinn SD; et al. Real-time probing of β-amyloid self- assembly and inhibition using fluorescence self-quenching between neighbouring dyes. Mol. Biosyst. 2014, 10, 34–44. [PubMed: 24170094]

(74). Lakowicz JR Quenching of Fluorescence. Principles of Fluorescence Spectroscopy; Springer US, 1983; pp 257–301. DOI: 10.1007/978-1-4615-7658-7_9.

(75). Stine WB; Jungbauer L; Yu C; Ladu MJ Preparing synthetic Aβ in different aggregation states. Methods Mol. Biol. 2010, 670, 13–32.

(76). Kroksveen AC; Opsahl JA; Aye TT; Ulvik RJ; Berven FS Proteomics of human cerebrospinal fluid: Discovery and verification of biomarker candidates in neurodegenerative diseases using quantitative proteomics. Journal of Proteomics 2011, 74, 371–388. [PubMed: 21111852]

(77). Lin D; et al. Investigation of the Dissociation Mechanism of Single-Walled Carbon Nanotube on Mature Amyloid-β Fibrils at Single Nanotube Level. J. Phys. Chem. B 2020, 124, 3459–3468. [PubMed: 32283926]

(78). Shipley MM; Mangold CA; Szpara ML Differentiation of the SH-SY5Y human neuroblastoma cell line. J. Vis. Exp. 2016, 2016, 53193.

(79). Krishtal J; Bragina O; Metsla K; Palumaa P; Tõugu, V. In situ fibrillizing amyloid-beta 1–42 induces neurite degeneration and apoptosis of differentiated SH-SY5Y cells. PLoS One 2017, 12, 12.

(80). Del Prete D; et al. Localization and Processing of the Amyloid-Protein Precursor in Mitochondria-Associated Membranes. J. Alzheimer's Dis 2016, 55, 1549–1570.

(81). Hu X; et al. Amyloid seeds formed by cellular uptake, concentration, and aggregation of the amyloid-beta peptide. Proc. Natl. Acad. Sci. U. S. A. 2009, 106, 20324–20329. [PubMed: 19910533]

(82). Shelton CC; Tian Y; Frattini MG; Li YM An exo-cell assay for examining real-time -secretase activity and inhibition. Mol. Neurodegener. 2009, 4, 22. [PubMed: 19490610]

(83). Shin J; Lee S; Cha M Neuroprotective effect of single-wall carbon nanotubes with built-in peroxidase-like activity against β-amyloid-induced neurotoxicity. Medchemcomm 2017, 8, 625–632. [PubMed: 30108779]

(84). Xue X; et al. Single-Walled Carbon Nanotubes Alleviate Autophagic/Lysosomal Defects in Primary Glia from a Mouse Model of Alzheimer's Disease. Nano Lett. 2014, 14, 5110–5117. [PubMed: 25115676]

(85). Park EK; et al. Optimized THP-1 differentiation is required for the detection of responses to weak stimuli. Inflamm. Res. 2007, 56, 45–50. [PubMed: 17334670]

(86). Morelli L; Giambartolomei GH; Prat MI; Castaño, E. M. Internalization and resistance to degradation of Alzheimer's Aβ1–42 at nanomolar concentrations in THP-1 human monocytic cell line. Neurosci. Lett. 1999, 262, 5–8. [PubMed: 10076859]

(87). Giri RK; Selvaraj SK; Kalra VK Amyloid Peptide-Induced Cytokine and Chemokine Expression in THP-1 Monocytes Is Blocked by Small Inhibitory RNA Duplexes for Early Growth Response-1 Messenger RNA. J. Immunol. 2003, 170, 5281–5294. [PubMed: 12734378]

(88). Yates SL; et al. Amyloid β and Amylin Fibrils Induce Increases in Proinflammatory Cytokine and Chemokine Production by THP-1 Cells and Murine Microglia. J. Neurochem. 2000, 74, 1017–1025. [PubMed: 10693932]

(89). Omtri RS; Davidson MW; Arumugam B; Poduslo JF; Kandimalla KK Differences in the Cellular Uptake and Intracellular Itineraries of Amyloid Beta Proteins 40 and 42: Ramifications for the Alzheimer's Drug Discovery. Mol. Pharmaceutics 2012, 9, 1887.

(90). Galassi TV; et al. Long-term in vivo biocompatibility of single-walled carbon nanotubes. PLoS One 2020, 15, No. e0226791.

(91). Illouz T; Madar R; Griffioen K; Okun E A protocol for quantitative analysis of murine and human amyloid-β1–40 and 1–42. J. Neurosci. Methods 2017, 291, 28–35. [PubMed: 28768163]

(92). Bramini M; et al. Graphene Oxide Nanosheets Disrupt Lipid Composition, Ca2+ Homeostasis, and Synaptic Transmission in Primary Cortical Neurons. ACS Nano 2016, 10, 7154–7171. [PubMed: 27359048]

(93). Ema M; Gamo M; Honda K A review of toxicity studies of single-walled carbon nanotubes in laboratory animals. Regul. Toxicol. Pharmacol. 2016, 74, 42–63. [PubMed: 26619783]

(94). Jiang T; et al. Toxicity of single-walled carbon nanotubes (SWCNTs): effect of lengths, functional groups and electronic structures revealed by a quantitative toxicogenomics assay. Environ. Sci. Nano 2020, 7, 1348–1364. [PubMed: 33537148]

(95). Williams AB; Schumacher B p53 in the DNA-Damage-Repair Process. Cold Spring Harb. Perspect. Med. 2016, 6, 6.

(96). Luo J; et al. The Aβ peptide forms non-amyloid fibrils in the presence of carbon nanotubes. Nanoscale. 2014, 6, 6720–6726. [PubMed: 24820873]

(97). Nicoll AJ; et al. Amyloid-β nanotubes are associated with prion protein-dependent synaptotoxicity. Nat. Commun. 2013, 4, 1–9.

(98). Miller Y; Ma B; Tsai CJ; Nussinov R Hollow core of Alzheimer's Aβ42 amyloid observed by cryoEM is relevant at physiological pH. Proc. Natl. Acad. Sci. U. S. A. 2010, 107, 14128–14133. [PubMed: 20660780]

(99). Necula M; Kayed R; Milton S; Glabe CG Small molecule inhibitors of aggregation indicate that amyloid beta oligomerization and fibrillization pathways are independent and distinct. J. Biol. Chem. 2007, 282, 10311–10324. [PubMed: 17284452]

(100). Puzzo D; et al. Endogenous amyloid-β is necessary for hippocampal synaptic plasticity and memory. Ann. Neurol. 2011, 69, 819–830. [PubMed: 21472769]

(101). Lazarevic V; et al. Physiological concentrations of amyloid beta regulate recycling of synaptic vesicles via alpha7 acetylcholine receptor and CDK5/calcineurin signaling. Front. Mol. Neurosci. 2017, 10, 10. [PubMed: 28197071]

(102). Tiiman A; Jarvet J; Gräslund A; Vukojevi V Heterogeneity and Turnover of Intermediates during Amyloid-β (Aβ) Peptide Aggregation Studied by Fluorescence Correlation Spectroscopy. Biochemistry 2015, 54, 7203–7211. [PubMed: 26574169]

(103). Schmittschmitt JP; Scholtz JM The role of protein stability, solubility, and net charge in amyloid fibril formation. Protein Sci. 2003, 12, 2374–2378. [PubMed: 14500896]

(104). Ryan TM; et al. Ammonium hydroxide treatment of Aβ produces an aggregate free solution suitable for biophysical and cell culture characterization. PeerJ. 2013, 1, e73. [PubMed: 23678397]

(105). Kuipers BJH; Gruppen H Prediction of Molar Extinction Coefficients of Proteins and Peptides Using UV Absorption of the Constituent Amino Acids at 214 nm To Enable Quantitative Reverse Phase High-Performance Liquid Chromatography-Mass Spectrometry Analysis. Journal of agricultural and food chemistry. 2007, 55, 5445–5451. [PubMed: 17539659]

(106). Tsai TW; et al. Adsorption of glucose oxidase onto single-walled carbon nanotubes and its application in layer-by-layer biosensors. Anal. Chem. 2009, 81, 7917–7925. [PubMed: 19788314]

(107). Roxbury D; et al. Hyperspectral Microscopy of Near-Infrared Fluorescence Enables 17-Chirality Carbon Nanotube Imaging. Sci. Rep. 2015, 5, 14167. [PubMed: 26387482]

(108). De Ferrari GV; Mallender WD; Inestrosa NC; Rosenberry TL Thioflavin T Is a Fluorescent Probe of the Acetylcholinesterase Peripheral Site That Reveals Conformational Interactions between the Peripheral and Acylation Sites. J. Biol. Chem. 2001, 276, 23282–23287. [PubMed: 11313335]

(109). Encinas M; et al. Sequential Treatment of SH-SY5Y Cells with Retinoic Acid and Brain-Derived Neurotrophic Factor Gives Rise to Fully Differentiated, Neurotrophic Factor-Dependent, Human Neuron-Like Cells. J. Neurochem. 2000, 75, 991–1003. [PubMed: 10936180]
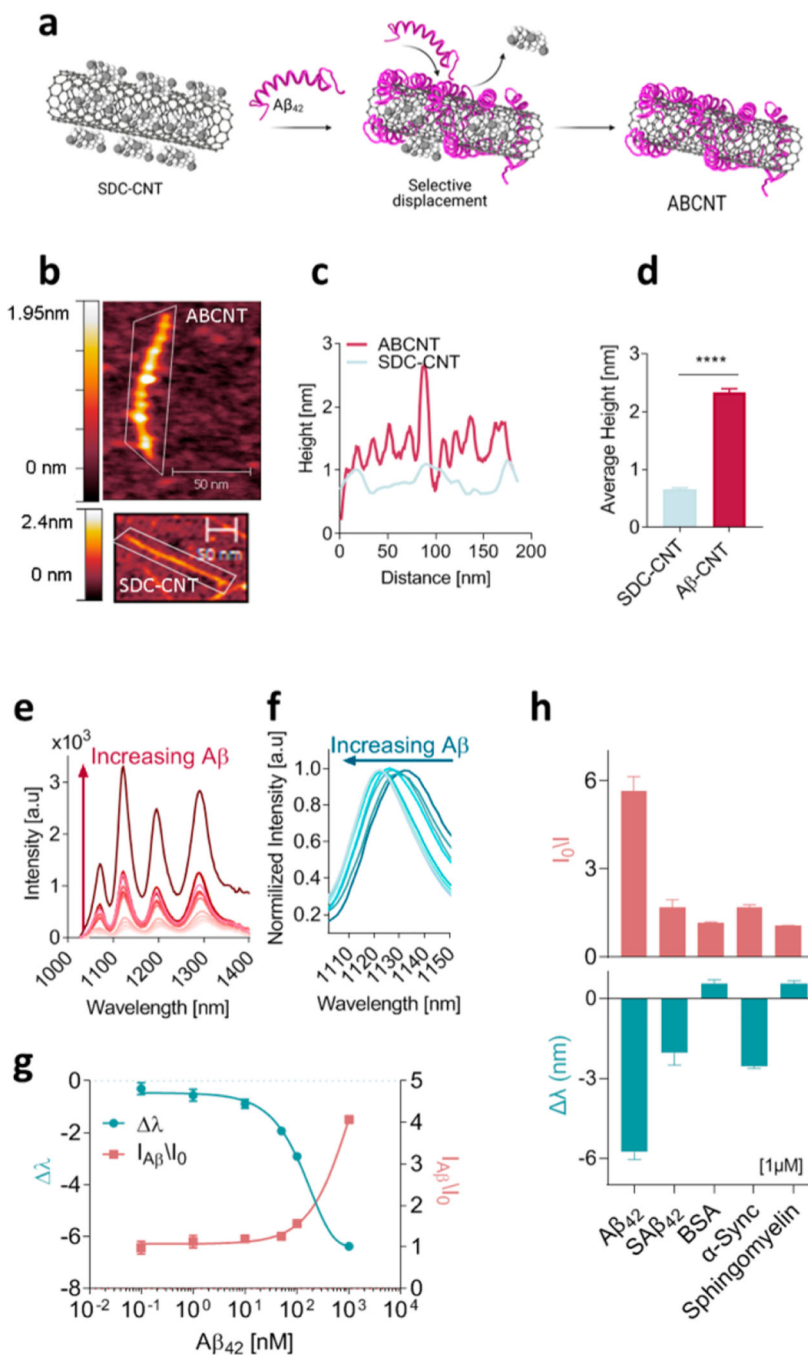
Figure 1. ABCNTs are nanoscale sensors for Aβ.
(a) Schematic illustration of Aβ-carbon nanotube (ABCNT) assembly via selective displacement. (b) Representative atomic force microscopy (AFM) image of an ABCNT and a sodium deoxy cholate-suspended carbon nanotube (SDC-CNT). Scale bar: 50 nm. (c) Height profiles of an ABCNT and SDC-CNT. (d) Average height of ABCNTs and SDC-CNTs, as derived from AFM images ($n = 42$ and 88 nanotubes, respectively). Error bars denote standard error, **** $p < 0.0001$ as measured via unpaired t test. (e) Emission spectra of ABCNTs exposed to increasing concentrations of Aβ$_{42}$ (1 nM to 10 μM). (f)

Normalized spectra from (e), focused on the (9,4) nanotube species. (g) Wavelength (λ, blue line) and intensity change ($I_{A\beta}/I_0$, pink lines) of ABCNTs exposed to increasing concentrations of $A\beta_{42}$. Data is fitted with one-phase decay model ($R_2 > 0.97$). Error bars represent standard deviation. $N = 3$ technical replicates. (h) Emission of the (9,4) ABCNT, in response to $A\beta_{42}$, scrambled $A\beta_{42}$ ($SA\beta_{42}$), bovine serum albumin (BSA), a synuclein (a-Sync) and sphingomyelin, each at 1 μM. Error bars = deviation for 3 technical replicates. ****$p < 0.0001$, as measured with a one-way ANOVA with Tukey's multiple comparisons test between groups.
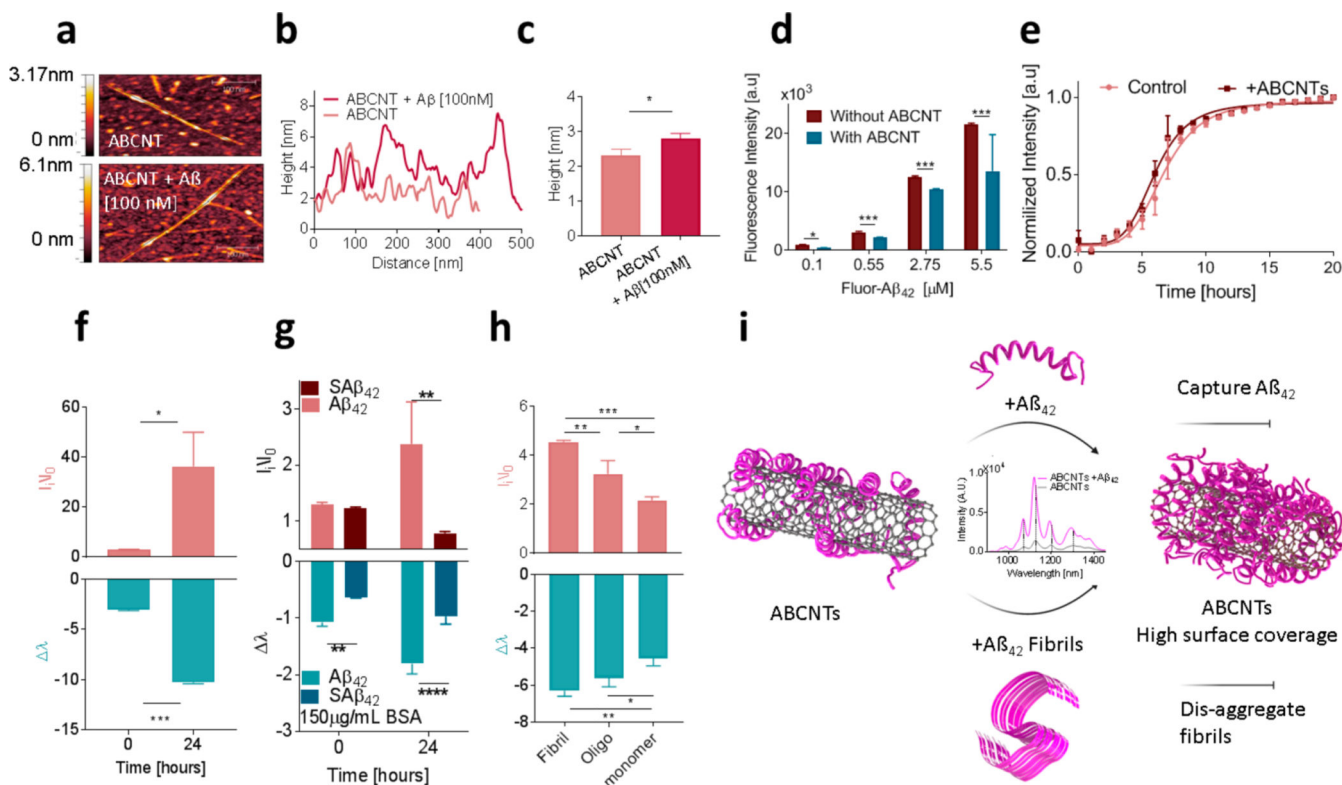
Figure 2. ABCNT Mechanism.

(a) Representative AFM images of ABCNTs (top) and after addition of freshly prepared Aβ_{42} [100 nM] (bottom). Scale bar = 100 nm. (b) Height profiles derived from AFM images. (c) Average ridge height of ABCNTs. Error bars = standard error of mean ($n > 75$). *$p < 0.05$ as measured by t test. (d) Intensity of fluorescent-Aβ (fluor-Aβ) in response to ABCNTs. Error bars = standard error of mean for three technical replicates, *$p < 0.05$, **$p < 0.01$, ***$p < 0.001$ as measured with one-way ANOVA with Tukey's multiple comparisons between groups. (e) Intensity of thioflavin-t (ThT) fluorescence of Aβ42 [10 μM] without (control) and with ABCNT [1 μg/mL]. Error bars = standard deviation of 3 technical replicates. ***$p < 0.001$ as measured with t test. (f) Change in intensity (top) and center wavelength (bottom) of ABCNTs incubated with freshly prepared Aβ_{42} [10 μm] at time 0 h and following 20 h incubation at 37 °C. Error bars = standard deviation for 3 technical replicates. ***$p < 0.001$, *$p < 0.05$ as measured with t test. (g) ABCNT response to Aβ_{42} [1 μM] and scrambled Aβ_{42} (SAβ_{42}) [1 μM] in BSA. Error bars = standard deviation for 3 technical replicates, **$p < 0.01$, ****$p < 0.0001$, as measured with two-way ANOVA with Sidak's multiple comparisons between groups. (h) ABCNT response to different Aβ_{42} aggregation states. Change in intensity (top) and center wavelength (bottom) of ABCNTs incubated with freshly prepared Aβ_{42}, oligomers, and fibrils [10 μM]. Error bars = standard deviation for 3 technical replicates. *$p < 0.05$,**$p < 0.01$, ***$p < 0.001$,****$p < 0.0001$, as measured with one-way ANOVA with Tukey's multiple comparisons between groups. (i) Schematic illustration of the proposed mechanism of action.
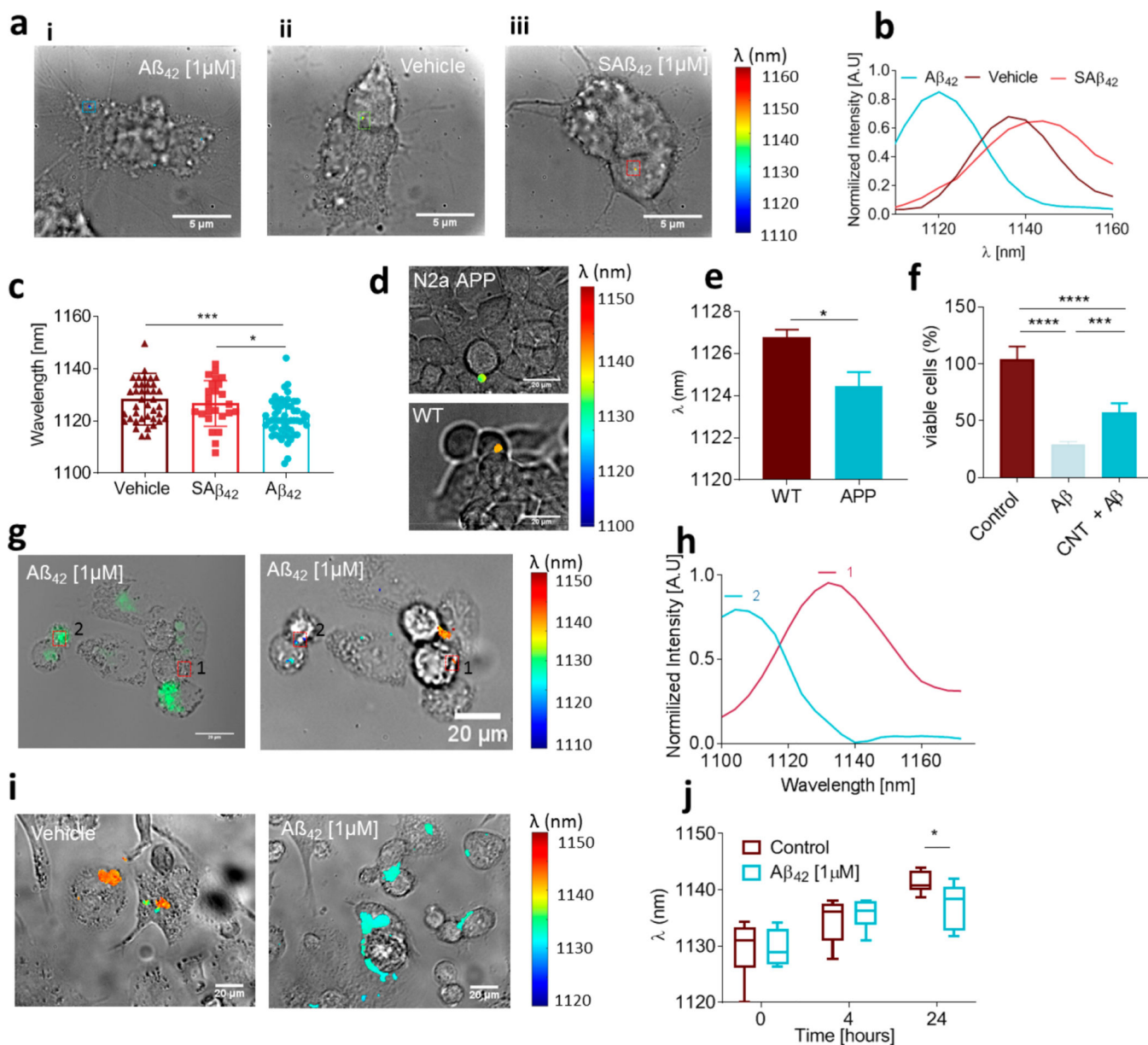
Figure 3. ABCNT detection of Aβ accumulation in live cells.
(a) Near-infrared hyperspectral maps of ABCNT emission wavelength overlaid with brightfield images of SH-SY5Y differentiated cells in response to (i) Aβ$_{42}$ [1 μM], (ii) vehicle only, or (iii) scrambled Aβ$_{42}$ [1 μM]. (b) Emission spectra of ROIs denoted on the images in (a). Spectra were smoothed and normalized. (c) Center wavelength of ABCNT emission in SH-SY5Y-differentiated cells from three individual biological replicates; error bars represent standard deviation. *$p < 0.05$, **$p < 0.01$ as measured with a one-way ANOVA with Tukey's multiple comparisons test between groups. (d) Near-infrared hyperspectral maps of ABCNT emission wavelength overlaid with brightfield images of N2a APP and N2a WT cells. (e) Center wavelength of ABCNT sensor (9,4) emission of N2a WT and N2a cells. Error bars = standard deviation of the mean of three biological replicates. *$p < 0.05$ as measured with t test. (f) Cell viability of N2a cells incubated with

ABCNT [1 μg/mL] and with Aβ_{42} [10 μM] for 72 h. Results of three technical replicates. Error bars = standard error. **$p < 0.01$, ***$p < .001$, ****$p < 0.0001$ as measured with a one-way ANOVA with Tukey's multiple comparisons test between groups. (g) (left) Fluorescence intensity of THP-1 cells incubated with fluorescently tagged Aβ_{42} [1 μM]. (right) Near-infrared hyperspectral maps of ABCNT emission wavelength in THP-1 cells. Both images are overlays on brightfield images of the cells. ROIs select regions with low intracellular Aβ content (1) and high intracellular Aβ content (2). Scale bar = 20 μm. (h) Corresponding emission spectra of ROIs from panel g. Spectra were smoothed and normalized. (i) Representative near-infrared hyperspectral maps of ABCNT emission wavelength overlaid with brightfield images of THP-1 cells incubated with vehicle (left) or Aβ_{42} [1 μM] (right) for 24 h. Scale bar = 20 μm. (j) Dynamic response of ABCNT sensor to intracellular accumulation Aβ_{42} in THP-1 cells, as measured via spectroscopy in 96 well plates. Results are from three biological repeats carried out in triplicate at least. Error bars = standard error. *$p < 0.05$ as measured with two-way ANOVA with Sidak's multiple comparisons test between groups.
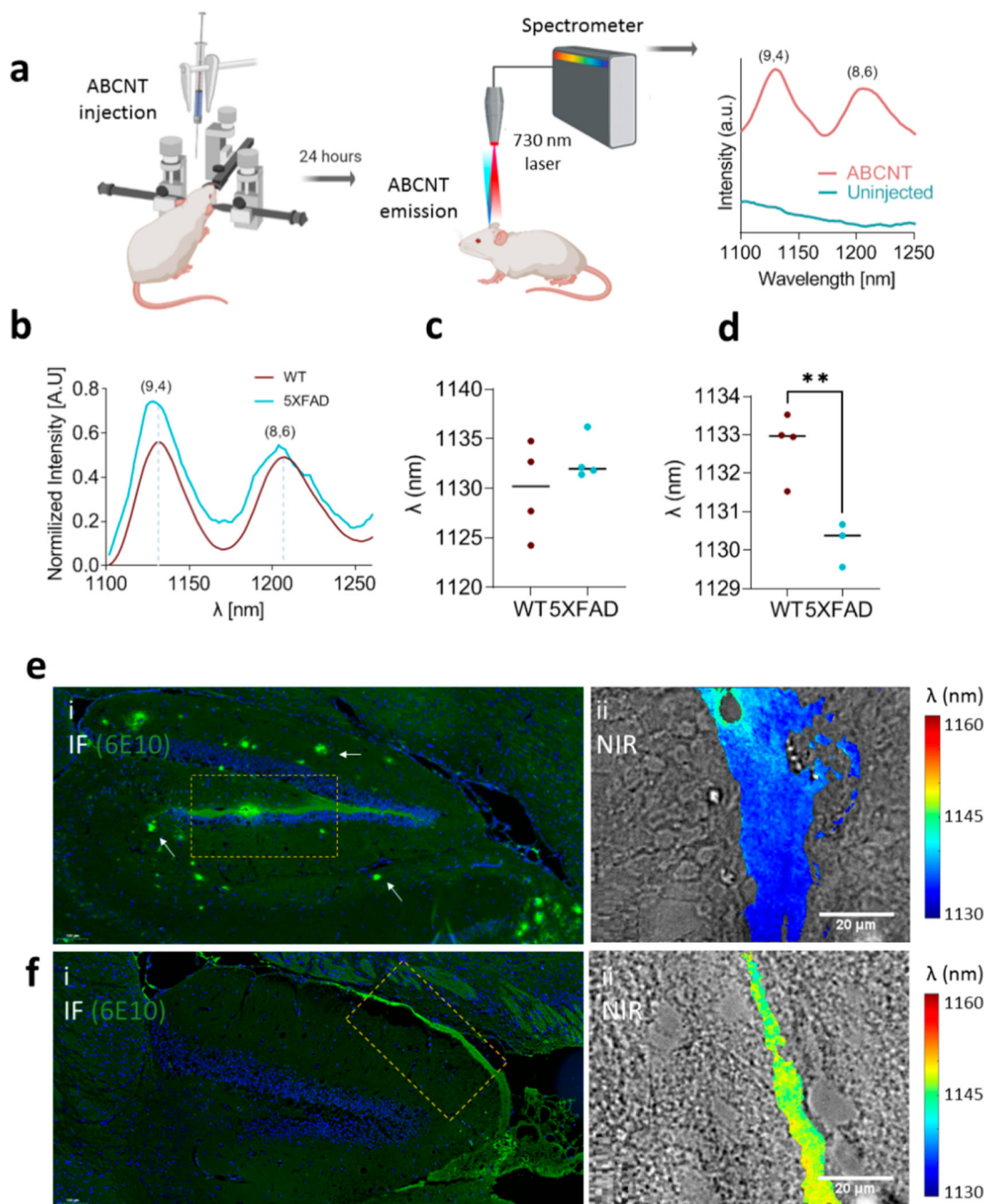
Figure 4. ABCNT intracranial optical response.
(a) (left) Schematic illustration of experimental procedure. (right) Near-infrared emission spectra of ABCNTs from within the live brain (ABCNT) and uninjected hemisphere control (uninjected). (b) Representative emission spectra acquired in vivo from 5XFAD and WT mice. (c) Mean center wavelength of ABCNT emission from WT and 5XFAD 4 month-old mice ((9,4) chirality). (d) Mean center wavelength of ABCNT emission from WT and 5XFAD 8-month old mice ((9,4) chirality). **$p < 0.001$ as measured with t test. Data points are from individual mice. (e) Hippocampal section from 8-month-old 5XFAD mouse. (i)

Immunolabeled section with 6E10 antibodies against Aβ (green) to detect ABCNT and Aβ aggregates (white arrow); DAPI (blue). Yellow box highlights a ROI containing ABCNTs. Scale bar = 100 μm. (ii) Near-infrared hyperspectral map of ABCNT emission wavelength derived from ROI in panel i. Scale bar = 25 μm. (f) Hippocampal section from an 8 month-old WT mouse. (i) Immunolabeled section with 6E10 antibodies against Aβ (green) to detect ABCNT and Aβ aggregates (white arrow); DAPI (blue). Yellow box highlights a ROI containing ABCNTs. Scale bar = 100 μm. (ii) Near-infrared hyperspectral map of ABCNT emission wavelength derived from ROI in panel i. Scale bar = 25 μm.